Chapter 6

THERMOHALINE CIRCULATION

1 Phenomenology and Processes

As discussed in Chap. 1, the global distribution of surface heat and water fluxes creates large-scale, upper-ocean pressure gradients and sparsely distributed sites of deep convection (mainly in Labrador, Greenland, Weddell, and Ross Seas) that combine to drive the global-scale thermohaline circulations (THCs). These surface forcings and the THC are also the cause of the stably stratified pycnocline structure found almost everywhere away from the deep convection sites. Here we continue the examination of the THC. We will see how an abyssal circulation can be driven by localized downwelling regions balanced by widespread upwelling over the rest of the ocean, as in the model by Stommel and Arons (1960). A component of this circulation is the Deep Western Boundary Currents (DWBC) that move away from the sinking regions, as well as along the equator. The signatures of this abyssal circulation are evident in the abyssal water-mass distributions. Another topic is the existence of multiple equilibria (*i.e.,* different steady circulation patterns) for the THC, with the implication of possible regime transitions in past and future climates. Yet another topic is basin-scale instabilities of the THC that lead to oscillations with decadal and longer periods. These oscillations are quite distinct from the mesoscale, barotropic and baroclinic shear instabilities of the wind-driven currents seen earlier in Chaps. 3-5. In addressing each of these topics, we will use simplified models, mostly, but not entirely, deferring until Chap. 7 further discussion of fully 3D circulation. (There is substantial overlap here with the topics in Welander (1986).)

In Chaps. 1 and 2 we have already seen various graphical depictions of the density stratification and THC:

- Typical pycnocline structure (Chap. 1, Fig. 1)
- Isentropic laminae and their topology on macro-, meso-, and microscales (Chap. 1, Fig. 11)
- Heat and freshwater forcing at surface (Chap. 2, Figs. 5, 7-10)
- THC as part of the global MOC (Chap. 1, Fig. 5)
- Meridional heat transport (Chap. 2, Fig. 4)
- Global "conveyor-belt" pattern for the THC (Chap. 1, Fig. 7)
- Abyssal penetrations of North Atlantic Deep Water (NADW) and Antarctic Bottom Water (AABW) in T, and S in the North Atlantic (Chap. 1, Figs. 8-9)

- Hydraulically controlled AABW flow through the Vema Gap (Chap. 1, Fig. 13)

The oceanic buoyancy forcing is, on the planetary scale, one of tropical heating and salinifying and polar cooling and freshening, although there is a sizable local freshening near the Intertropical Convergence Zone (*i.e.,* ITCZ; Chap. 2, Figs. 9-10). Since these have opposing effects on the surface density, hence on the meridional buoyancy gradients, we can anticipate delicate balances and exotic responses in the THC. These forcings imply that there must be mean poleward fluxes of warm, salty water and equatorward return flows of cool, fresh water (Fig. 1). The largest sustained air-sea fluxes occur near the largest gyre currents, because they are capable of large lateral advective transports of heat that can resupply these sites of large vertical flux; note in particular the regions around the Gulf Stream, the Antarctic Circumpolar Current, the Agulhas Current, and the Equatorial Currents. However, these are not the sites of deep convection, which are in locations where the lateral flux of lighter water is relatively weak, so that negative buoyancy fluxes that are even rather modest in amplitude can suffice to make the surface waters heavy enough to sink and convect deeply.

The stable vertical density stratification is mostly the product of the isopycnal mixing away from the boundaries and the elevated diapycnal mixing in and near the surface and bottom boundary layers (Fig. 2). Significant mixing occurs in turbulent gravity currents (Fig. 6) where denser water flows downhill (*e.g.,* the Mediterranean Outflow and Iceland-Faroe Sill Overflow) and sometimes in connection with the turbulence around hydraulic control points. The interior material mixing rates are believed to be governed by small-scale waves and turbulence, *viz.,* breaking inertia-gravity waves, Kelvin-Helmholtz instability, and double diffusion, with different efficiencies in different locations. A currently popular hypothesis is that both tidal currents in shallow water and tidally generated inertia-gravity waves in the deep ocean over topography are potentially important sources of mixing, especially in the abyssal water beneath the pycnocline (Munk and Wunsch (1998); also see Chap. 4, Appendix Chap. 4, (Webb and Suginohara, 2001)). Measurements of diapycnal mixing have been mainly by indirectly inference from microstructure, but in the past decade purposeful tracer releases have provided direct evidence (Figs. 3-4, further discussed in Sec. 2.2).

Water masses that go into the abyss (a.k.a. deep water) are formed in several places: in the ocean ocean, usually in association with cyclonic *preconditioning* flows (Fig. 7); in shallow regions on continental shelves (*e.g.,* in parts of the Weddell Sea); and in marginal seas with sills that are partial barriers to the world ocean (*e.g.,* the Mediterranean Sea). In Fig. 8 we see that the circulation of the Labrador Sea is generally cyclonic, and the deepest winter convection occurs in a rather small region in its center where its isopycnals bulge upward, and consequently the interior stratification is weakest. From shallow or marginal sources, the associated dense water subsequently flows off the shelf or over the sill and then down a bottom slope into the abyss. This way of renewing deep water masses is sketched in Fig. 5, and a closer look at the flow in a down-slope gravity current is in Fig. 6.

The net result of having geographically localized, deep-water formation sites is that they are

usually distinguishable in their characteristic chemical signatures. These distinctive *water masses* have long been known because they are so readily measurable by hydrography. Figures 9-18 illustrate various water mass features, and they are further discussed in Sec. 2.3.

2 Simple Models of the THC

The oceanic THC occurs under many influences, including complex patterns for the buoyancy fluxes and the basin shapes; coupling with the wind driven circulations; and subtleties of the equation of state at low temperature where the linearized approximation (Chap. 1) is least reliable. As a result full OGCM solutions (Chap. 7) are an important means of investigating the THC. Nevertheless, there are several simpler models we will consider that are useful in understanding basic THC dynamics.

2.1 Maintenace of the Pycnocline

The time-averaged buoyancy balance outside of the boundary layers has the adiatatic form,

$$\mathbf{u} \cdot \boldsymbol{\nabla} b \;=\; -\boldsymbol{\nabla} \cdot \overline{\mathbf{u}' b'} \,, \tag{1}$$

neglecting compressibility and molecular diffusion. Here an overbar is implicit for the mean fields on the left-hand side of (1). The theory of Gent and McWilliams (1990) posits that the largest eddy fluxes in (1) are due to mesoscale eddies; they act in an integrally adiabatic fashion to move the mean isopycnal surfaces around as part of the shaping of the main pycnocline. The parameterization form is expressed as a Lagrangian mean advection,

$$\boldsymbol{\nabla} \cdot \overline{\mathbf{u}' b'} \;=\; \mathbf{u}_* \cdot \boldsymbol{\nabla} b \,, \tag{2}$$

where $\mathbf{u}_*$ is the non-divergent, eddy-induced transport velocity (also in Chaps. 3-4). Historically, however, the oceanographic theories of the pycnocline have focused on an alternative approximate balance for (1), *viz.,*

$$\mathbf{u} \cdot \boldsymbol{\nabla} b \;=\; -\left[\kappa_v b_z\right]_z \,, \tag{3}$$

which, in particular, is the basis for the so-called *thermocline theory* (Sec. 3.1). This balance neglects the effects of mesoscale eddies and includes the vertical mixing caused by microscale motions such as breaking internal gravity waves, Kelvin-Helmholtz shear instability, and double diffusion. If the issue is how the pycnocline surface is bent and moved around, then the mesoscale effects in (2) may be very important; however, if the issue is how the pycnocline is formed and how heat and salt cross it between tropical and polar regions, then the microscale effects in (3) are essential.

An experiment was made in the pycnocline of the North Atlantic sub-tropical gyre, in which a "dye" of SF_6 was released in a small patch centered about a particular buoyancy surface. SF_6

does not occur naturally and thus is a controlled tracer (although by now enough releases have been made in both the ocean and atmosphere that its controllability is diminishing). Over time the dye was stirred laterally on the surface by mesoscale eddies and mixed vertically across it by microscale motions, and the resulting dye distributions were measured (Figs. 3-4). The diapycnal spreading was fit to a 1D conduction equation,

$$\frac{\partial c}{\partial t} \;=\; \kappa_v \frac{\partial^2 c}{\partial z^2}\,,$$

with a best-fit eddy diffusivity value of $\kappa_v \;=\; 2\times 10^{-5}$ m^2 s^{-1} (Fig. 4). This is much larger than the molecular values of 10^{-7} m^2 s^{-1} for heat and 10^{-9} m^2 s^{-1} for salt, but it is still smaller, by about an order of magnitude, than was earlier believed when (3) was viewed as the controlling dynamical balance for the pycnocline (Munk, 1966). This dye-determined value is consistent with other, less direct, recent empirical estimates of κ_v in the pycnocline, although many of them are even smaller by a factor of 2-5. This range of values is explained, in part, by geographical variations in the occurrence of double diffusion (thought to be relative strong at the site for Fig. 4). Another dye experiment occurred in the Brazil Basin's abyssal waters the over rough topography associated with the mid-Atlantic ridge. Its results indicated a larger best-fit value of $\kappa_v \;\approx\; 10^{-4}$ m^2 s^{-1}. This abyssal increase in κ_v is thought to be primarily a consequence of two processes:

1. Relatively large diapycnal fluxes in the bottom PBL where it intersects iso-buoyancy surfaces, with efficient mesoscale fluxes carrying the tracers to and from the boundaries along the iso-buoyancy surfaces (Fig. 2).

2. Upward interal gravity wave radiation from flow past topography, followed by steepening, breaking, and mixing events as the waves encounter larger stratification and horizontal current shear (*e.g.,* providing critical layers where the phase speed is equal to the current speed); the generating current can be either the tides or the circulation, and the present observational evidence is that this enhanced deep mixing is quite inhomogeneously distributed.

These pathways are not as available in the upper ocean where a typical distance to the nearest solid boundary intersection is much greater and where bottom-generated gravity waves do not penetrate as readily. Note that the upper-ocean, dye-measured value of κ_v implies a full-column diffusive adjustment time of $H^2/\kappa_v \;=\; 4.5\times 10^{11}$ s$=\; 1.4\times 10^4$ yr for a vertical scale of $H = 3000$ m, although the adjustment time is shorter for smaller values of H characteristic of the thermocline. A value of κ_v ten times bigger implies a full-column diffusion time of 10^3 yr. This deep diapycnal mixing well away from isopycnal intersections with the solid bottom is believed to be the slowest process involved in bringing the ocean into equilibrium with a steady surface forcing field or with climate variability over intervals shorter than the ice ages.

2.2 1D Advection-Diffusion Balance

We now make a scaling analysis of (3). Assume that it is accompanied by geostrophic, hydrostatic balance, which implies

$$\frac{fV}{H} \sim \frac{\Delta b}{L}, \tag{4}$$

and a 3D continuity balance, which implies

$$\frac{W}{H} \sim \frac{V}{L}. \tag{5}$$

Together these relations imply

$$W \sim \frac{\Delta b}{f(H/L)^2}. \tag{6}$$

Another scaling balance comes from (3), *viz.,*

$$\frac{U\Delta b}{L} \sim \frac{W\Delta b}{H} \sim \frac{\kappa_v \Delta b}{H^2}. \tag{7}$$

These latter two relations imply

$$H \sim \left(\frac{\kappa_v f L^2}{\Delta b}\right)^{1/3}, \quad W \sim \left(\frac{\kappa_v^2 \Delta b}{f L^2}\right)^{1/3}. \tag{8}$$

This is a scaling estimate for the depth scale of the thermocline and its associated mean circulation. If we use characteristic scales of $\Delta b = 0.02$ m s^{-2}, $f = 10^{-4}$ s^{-1}, $L = 10^7$ m (planetary scale), and $\kappa_v = 10^{-5}$ m^2 s^{-1}, then from (8) we predict $H \sim 200$ m and $W \sim 6 \times 10^{-8}$ m s$^{-1} = 2$ m yr^{-1}. These values are of the right order of magnitude, although both are a bit small compared to the observed thickness of the pycnocline in most places and, say, the Stommel-Arons estimate (below) for the uniformly distributed upwelling at the base of the pycnocline. Notice from (8) that this discrepancy would be less if κ_v were larger, as it once was believed to be everywhere and has now been found only in some places in the abyssal ocean where steep topography supports the generation of strong internal tidal oscillations (Munk, 1966; Munk and Wunsch, 1998). Nevertheless, (8) is qualitatively reasonable. It also encourages us to view the pycnocline as a vertical boundary layer.

We can pursue this idea further if we further restrict (3) to a 1D advection-diffusion balance,

$$w\frac{\partial b}{\partial_z} = \kappa_v \frac{\partial^2 b}{\partial_z^2}. \tag{9}$$

If we assume w and κ_v are constants, then (9) has a boundary-layer solution of the form

$$b = b_o \exp\left[\frac{z - z_o}{h}\right], \tag{10}$$

for $z < z_o$ and $h = \kappa_v/w > 0$. This solution is consistent with the scaling theory (8), but it is also less restrictive because it can also accommodate general values of $\kappa_v > 0$ and $w > 0$. The latter requirement means that this view of the pycnocline is only valid where there is upwelling, $w > 0$. Almost universal upwelling is, of course, one of the premises of the Stommel-Arons theory (Sec. 2.3), but it is consistent with the sign of the wind-forced Ekman pumping only over about half the globe (mostly in the sub-polar gyres). So, at the least, there must be some mutual accommodation in the upper pycnocline between the Ekman pumping at the base of the Ekman layer and the pycnocline upwelling. In reality, this doesn't leave much room to maneuver. It probably is best to view (9) as only qualitatively relevant, with the real ocean in a more fully 3D mean buoyancy balance, with respect to both mean advection and eddy rectification, as in (1)-(3).

2.3 Abbysal Circulation and Stommel-Arons Theory

Since the traditionally most feasible technique for making ocean measurements is sampling of the material properties (Chap. 1), a traditional way of empirically characterizing the ocean has been by inferring circulation from the 3D spatial distributions of T, S, and other chemical concentrations that are approximately conserved following fluid parcels (or, as with radioactive decay, have known rates of change). Implicit in this inference are the following assumptions:

1. The surface chemical fluxes have large geographical contrasts with distinctive combinations for their tracer constituents.
2. The forcing and circulation are steady.
3. The material mixing rates are slow enough that geographical contrasts can persist over the many decades and centuries that parcels take to move significant distances around the ocean.

None of these assumptions is strictly correct, but experience has shown that they are all true enough for there to be significant information about circulation patterns in the water-mass distributions. Nevertheless, inferences of this type are difficult to defend as accuracte.

Examples of the spread of two different water masses from their source regions, NADW and AABW, respectively, are shown in Fig. 10. There are indications in the spreading patterns of a mid-depth DWBC in the NADW and of both a bottom DWBC as well as passage-following currents in the AABW. Figure 15 shows a geographical water-mass regime diagram for a zonal section in the sub-tropical North Atlantic. Figures 11-12 show tracer evidence of DWBC far away from deep-water formation sites: southward DWBC in the South Atlantic and northward in the South Pacific. Figure 9 shows meridional sections of tracers in the Atlantic, suggesting tongues of transported material in patterns that mirror the meridional overturning streamfunction (Fig. 5 of Chap. 1). Figure 13 shows the transient invasion of radioactive products from atmospheric nuclear bomb tests in the 1960s, showing the tracer penetration pathway from the sub-polar North Atlantic to

great depths in less than a decade, followed by southward advection by the THC. Figure 14 shows the decadal penetration of another transient tracer, Chlorofluorcarbons (CFCs; *e.g.,* freons), industrially produced in the middle of the century primarily for use in refrigeration. Along a mid-depth isopycnal surface (within the NADW), the CFCs move south in a DWBC, with a substantial part diverted to flow along the equator. Figure 16 has meridional cross sections showing the equatorial confinement and eastward penetration of the CFCs. An argument rationalizing the latter is that potential vorticity must change sign in order to cross the equator because f does; however, in the absence of rectification effects, potential vorticity should be conserved along large-scale trajectories lying within surfaces of constant potential density, and the trajectories must avoid crossing the equator for any significant distance. Since obviously some parcels do cross the equator, they must undergo significant mixing *en route* for q and other material tracers like freon.

How are we to understand the occurrence of DWBC? The original theory for this is by Stommel and Arons (1960), and an example of its solutions is shown in Fig. 18, where a global pattern of abyssal circulation, including several DWBC, arises from the assumption that there are deep-water formation (*i.e.,* deep convection) sites only in the Greenland and Weddell Seas. Note the absence of any eastward diversion of boundary currents crossing the equator; in this theory it is assumed that the western boundary currents are as diffusive as they need to be to satisfy the interior flow constraints (*n.b.,* this is somewhat analogous to the assumptions in the Sverdrup theory for wind-driven gyres).

The Stommel-Arons (S-A) problem assumes that the abyssal ocean is a shallow layer of uniform density, with depth H and with a steady circulation driven by a spatially concentrated mass source (with $w < 0$) and a uniformly distributed upwelling sink (with $w > 0$) everywhere else. This is, of course, a strong idealization for the abyssal thermohaline circulation in a number of ways (*e.g.,* by neglecting unsteadiness, rectification, topography, stratification, dynamical coupling with the upper ocean where the THC buoyancy forcing really occurs, and non-uniformly distributed $w(\lambda, \psi, z_o) > 0$). Nevertheless, there is often widespread appreciation for simple theories that seem to capture important phenomena with the least complexity, and the S-A problem has this virtue for the occurrence of DWBC.

Consider a simple basin geometry that is a hemispheric sector bounded by the equator and north pole, with latitudes $\phi = 0$ and $\pi/2$, and by the latitudes λ_w and λ_e (Fig. 17). Assume there is a downwelling volume flux S_o at the pole, with a integral mass balance determined by

$$S_o \;=\; Q_o \cdot Area \;=\; Q_o a^2 \, \Delta\lambda \,, \tag{11}$$

where $w \;=\; Q_o$ is the spatially uniform vertical upwelling velocity; a is the radius of the Earth; and $\Delta\lambda = (\lambda_e - \lambda_w)$ is the longitudinal width of the basin. The dynamics in the fluid interior (*i.e.,* away from the lateral boundaries and the source region) are geostrophic and hydrostatic balances

and 3D continuity, here expressed in spherical coordinates:

$$\begin{aligned} 2\Omega \sin\phi \, v &= \frac{1}{a\cos\phi} P_\lambda \\ 2\Omega \sin\phi \, u &= -\frac{1}{a} P_\phi \\ u_\lambda + [\cos\phi \, v]_\phi &= -a\cos\phi \, w_z \\ &= -\frac{aQ_o}{H}\cos\phi \, . \end{aligned} \tag{12}$$

The final line comes from matching $w(0) = Q_o$ and $w(-H) = 0$ with a linear function in z, since the Taylor-Proudman theorem applies here (*i.e.,* a rapidly rotating, uniform density, inviscid fluid has depth-independent horizontal motion, hence vertical motion that is a linear function of depth).

The solution to (12) is perhaps easier to verify than to derive; nevertheless, its horizontal velocity is

$$v \; = \; \frac{aQ_o}{H}\tan\phi \, , \tag{13}$$

which has $v = 0$ at $\phi = 0$ and $v \to \infty$ as $\phi \to \pi/2$, and

$$u_\lambda \; = \; -[\cos\phi \, v]_\phi - \frac{aQ_o}{H}\cos\phi \, , \tag{14}$$

or, after using the now-familiar choice of an eastern boundary condition with $u(\lambda_e, \phi) = 0$,

$$u \; = \; \frac{a}{H\tan\phi} \; [\lambda_e - \lambda] \; \frac{\partial Q_o \sin^2\phi}{\partial \sin\phi} \, . \tag{15}$$

Note that $u > 0$ everywhere, which indicates that the interior abyssal circulation is supplied from the western boundary current. Also note that $v > 0$ everywhere in the interior, even though the source is at the north pole. Thus, the interior flow represents a recirculation that converges on the source point at the pole and adds to the lateral transport carried by the DWBC. To connect the source flow with the interior flow, the DWBC transport at each latitude is assumed to exactly supply the volume transport required for all the interior upwelling that occurs more distantly from the source, detraining fluid as it progresses to the south. This northward DWBC transport can therefore be calculated at each latitude as the sum of total source strength (*i.e.,* $-S_o$ northward flow) minus the interior transport across the latitude line plus the interior upwelling to the north of the line:

$$\begin{aligned} T &= -S_o - \int_{\Delta\lambda} d\lambda \, aHv\cos\phi + Q_o a^2 \Delta\lambda \, (1 - \sin\phi) \\ &= Q_o a^2 \, \Delta\lambda - \Delta\lambda \, a^2 Q_o \sin\phi + Q_o a^2 \Delta\lambda \, (1 - \sin\phi) \\ &= -2Q_o a^2 \, \Delta\lambda \sin\phi \\ &= -2S_o \sin\phi \, . \end{aligned} \tag{16}$$

In this solution, $T \leq 0$ everywhere. It goes to zero at the equator, consistent with no upwelling at the equator and no cross-equatorial flow (unlike nature). Notice that T is twice as large as the source at the pol, because of lateral recirculation (see Fig. 17 for the lateral circulation pattern of (13)-(15)). This interior solution, like the wind-driven Sverdrup solution, can be completed with western boundary layers supported by lateral momentum diffusion.

Some typical numerical values for an oceanic realization of such a S-A circulation are $H = 4$ km; $S_o = 10$ Sv $= 10^7$ m^3 s^{-1}; $\Delta\lambda = 70^o = 1.22$ radians; $a = 6.35 \times 10^6$ m; $Q_o = 2 \times 10^{-7}$ m s^{-1} = 6 m yr^{-1}; and $v = 2 \times 10^{-4}$ m s^{-1}. In spite of this slow speed, the THC — with the S-A circulation as its abyssal component in the interior — is the dominant circulation type for global ocean heat transport.

The preceding A-A solution is a steady one. The behavior of its set-up — in a two-hemisphere sector domain and a variable upper interface height for the abyssal layer — is shown in Fig. 19, leading to the steady-state circulation in Fig. 20 after sufficient time elapses. The dynamical mechanism for the spin-up of the abyssal circulation involves both Kelvin and Rossby waves. The Kelvin waves propagate cyclonically around the boundary away from the equator (*i.e.,* in opposite directions in the two hemispheres) and eastward along the equator (Chap. 5).

Since both the Munk and Stommel-Arons theories are linear, they can formally be superimposed, although neither theory addresses the questions: What determines the vertical distribution of the wind-driven currents? What establishes and maintains the pycnocline (*i.e.,* the top of the S-A abyssal layer)? And what localizes the deep convection? In this traditional simple view, the wind gyres were assumed to be confined within the upper ocean, in and above the pycnocline. Since OGCM solutions show similar circulation patterns, we can infer from them, as well as more idealized problems, what the missing dynamical elements are for these simpler problems. The occurrence of the pycnocline and localized sinking regions are the result of a full-depth, nonlinear posing of the thermohaline circulation with laterally-varying surface fluxes, and the depth confinement of mean wind gyres is a result of the inefficiency of lateral buoyancy flux and isopycnal form stress (*i.e.,* vertical momentum flux) by mesoscale eddies in the weakly stratified abyssal water (Chaps. 3-4).

2.4 Box Models

A remarkably simple analog model of the THC was devised in Stommel (1961) (Fig. 21). It consists of two "boxes" within which the water is well-mixed. Each of the boxes is forced by an osmotic exchange with different external reservoirs (*i.e.,* the analog of surface fluxes), and the boxes exchange fluid through connecting pipes with a circulation transport rate proportional to the

buoyancy difference between them. The governing equations are

$$\begin{aligned} V_p\dot{T}_p &= C_{Tp}(\hat{T}_p - T_p) + |\Psi|(T_e - T_p) \\ V_e\dot{T}_e &= C_{Te}(\hat{T}_e - T_e) - |\Psi|(T_e - T_p) \\ \dot{S}_p &= C_{Sp}(\hat{S}_p - S_p) + |\Psi|(S_e - S_p) \\ V_e\dot{S}_e &= C_{Se}(\hat{S}_e - S_e) - |\Psi|(S_e - S_p) \\ \Psi &= -D[-\gamma_T(T_e - T_p) + \gamma_S(S_e - S_p)]\,. \end{aligned} \tag{17}$$

Here the boxes have volumes V, heat and saline capacities C, reservoir values $(\hat{T}, \hat{S})$, thermal expansion and haline contraction coefficients (γ_T, γ_S), and a circulation transport efficiency expressed as a diffusivity times a box length, D. The subscripts e and p invite the interpretation of the boxes as polar and equatorial regions, respectively. The exchange does not depend upon the sign of the circulation, since we assume it must be closed between only these two boxes; ***i.e.,*** for a flow from $e \to p$, there must also be a mass-balancing return flow from $p \to e$.

Now analyze (17) for its steady states, since the only transient behavior for steady reservoir values is relaxation to a unique steady state at rates $R = C/V$ (and if $C \propto V$ as usual, the R values are the same for the two boxes). The volumetric sum of the box (T, S) values relaxes to the volumetric sum of the reservoir values, since the circulation terms in (17) cancel when added and the relevant equations are linear. The more interesting variables are the differences between the boxes,

$$\Theta = T_e - T_p, \quad \Sigma = S_e - S_p\,. \tag{18}$$

We choose the following units for non-dimensionalization: $1/R_T$ for time, $(1/V_p + 1/V_e)^{-1}R_T/D\gamma_T$ for T, $(1/V_p + 1/V_e)^{-1}R_S/D\gamma_S$ for S, and $(1/V_p + 1/V_e)^{-1}R_T$ for Ψ. The dimensionless model is thus

$$\begin{aligned} \dot{\Theta} &= \alpha - \Theta - |\Psi|\Theta \\ \dot{\Sigma} &= \beta - \xi\Sigma - |\Psi|\Sigma \\ \Psi &= \Theta - \Sigma\,, \end{aligned} \tag{19}$$

where $\xi = R_s/R_T$, $\alpha = \hat{T}_e - \hat{T}_p$, and $\beta = \xi(\hat{S}_e - \hat{S}_p)$ are the three dimensionless control parameters. We are interested mostly in the regime $\xi < 1$, because we believe the climate-feedback (***i.e.,*** reservoir-exchange) rate is quicker for temperature than for salinity in nature.

The equilibria of this simple model are given by

$$\Theta = \alpha/(1 + |\Psi|), \;\; \Sigma = \beta/(1 + |\Psi|)\,,$$

and the solution of an implicit equation for Ψ,

$$\Psi(1 + |\Psi|)(\xi + |\Psi|) = \alpha(\xi + |\Psi|) - \beta(1 + |\Psi|)\,. \tag{20}$$

This is a cubic equation, and, under some conditions including $\xi \neq 1$, it can have multiple solutions (***i.e.,*** multiple equilibria). In the control space of forcing strengths (α, β), there is a line is a line

of zero circulation, $\beta = \xi\alpha$. There is a regime of multiple stable equilibria for forcing amplitudes bounded away from zero — *i.e.,* with appreciable nonlinearity in (20) — and lying between the zero-circulation line f_1 and another curve f_2 that lies above it for $\xi < 1$ (Fig. 22a). Outside of these lines there are only single equilibria. For $\hat{T}_p < \hat{T}_e$ and $\hat{S}_p < \hat{S}_e$ (as in nature), these two equilibria have either $\Psi > 0$, with polar "sinking" in the sense of the thermal driving, or $\Psi < 0$, with equatorial "sinking" in the sense of the salinity driving; we refer to these equilibria as TH and SA, respectively. At each of the curves f_1 and f_2, either the SA or TH equilibrium loses stability in what are called saddle-node bifurcations where two equilibrium solutions coalesce. Between these curves there are three equilibria, only two of which are stable (TH and SA). For $\xi < 1$ in the regime with both TH and SA solutions, the circulation strength is stronger in TH than in SA. Thus, this simple analog model has the property that the THC can occur in different circulation configurations, even with the same forcing fields (represented here by the reservoir values).

Additional variants have been proposed for simple models in the spirit of the 2-box model (Welander, 1986; Thual and McWilliams, 1992).

2.5 2D Models

Box-model solutions are, of course, not necessarily like fluid dynamical solutions. So now we consider the fluid dynamics of the 2D meridional-plane Boussinesq equations in a domain of size $L \times D$,

$$\begin{aligned} \frac{D\mathbf{u}}{Dt} &= -\boldsymbol{\nabla}\phi - \hat{z}g(-\gamma_T T + \gamma_S S) + \nu\nabla^2\mathbf{u} \\ \boldsymbol{\nabla}\cdot\mathbf{u} &= 0 \\ \frac{DT}{Dt} &= \kappa_T\nabla^2 T \\ \frac{DS}{Dt} &= \kappa_S\nabla^2 S\,, \end{aligned} \tag{21}$$

with $u = \partial_x = 0$. Note that the Coriolis force is absent here, and we have assumed, for simplicity, that the diffusive terms are isotropic (unlike in the ocean), although the domain is not isotropic (like the ocean). We make these equations non-dimensional with the following units: D for length, $2\pi D^3/L\kappa_T$ for time, $L\kappa_T/2\pi D^2$ for velocity, $\nu\kappa_T L^2/(4\pi^2 D^5 g\gamma_T)$ for temperature, and $\nu\kappa_T L^2/(4\pi^2 D^5 g\gamma_S)$ for salinity. Because of 2D non-divergence we can represent the velocity in terms of a meridional overturning streamfunction $\Psi(y,z)$,

$$v \;=\; -\Psi_z\,, \quad w \;=\; \Psi_y\,, \tag{22}$$

and replace the first two equations in (21) with the zonal vorticity equation. The resulting equation set is

$$\begin{aligned} (k\sigma)^{-1}\left[\nabla^2\Psi_t + J[\Psi,\nabla^2\Psi]\right. &= k^{-1}\left(T_y - S_y\right) + \nabla^4\Psi \\ k^{-1}\left[T_t + J[\Psi,T]\right. &= \nabla^2 T \\ k^{-1}\left[S_t + J[\Psi,S]\right. &= \tau\nabla^2 S\,, \end{aligned} \tag{23}$$

where $\sigma = \nu/\kappa_T$ is the Prandtl number, $\tau = \kappa_S/\kappa_T$ is the Lewis number, and $k = 2\pi D/L$ is the fundamental horizontal wave number in the domain. We take as boundary conditions on T and S the so-called "mixed" set,

$$T \;=\; a\cos ky, \quad S_z \;=\; b\cos[ky]\,, \tag{24}$$

at the top, with insulation conditions (*i.e.,* no flux) at the sides and bottom. a and b can each be thought of as a Rayleigh number, $\frac{\Delta}{\nu\kappa g\gamma H^3}$, associated with the strength Δ of the surface forcing for T and S, respectively. The conditions (24) reflect the physical view that the ocean surface temperature is tightly constrained due to efficient local feedbacks with the atmosphere, whereas salinity has a climatological flux independent of the local oceanic value. The forms in (24) are symmetric about the equator (at $y = 0$) and have the same equator vs. pole sense as in the true climatological forcing of the THC. For the velocity field we choose no normal flow and no stress at all boundaries, $\Psi \;=\; \Psi_{nn} \;=\; 0$.

We focus on the steady states of (23)-(24). In these equations (a, b, k, σ, τ) are the control parameters, but common practices in using OGCMs support the simplifications $\tau = 1$ and $\sigma \to \infty$, which reduces the control space to 3 parameters. We are interested in the regime $k < 1$ since oceanic basins are anisotropic (although this effect is partly canceled by the opposing anisotropy of the vertical and horizontal eddy diffusivities). We can show that the line $b \;=\; ak\tanh k$ is a line in the forcing space on which the circulation can vanish; this is most easily derived in the limit $a, b \to 0$, when the solution is linear and unique, but it also applies to arbitrary forcing values.

As expected from the 2-box analog model, this problem also has multiple equilibria for finite values of a and b (Fig. 23). Some of them retain the equatorial symmetry of the forcing; again we name name these solutions TH and SA. A comparison of their regime diagram with the 2-box model's is shown in Fig. 22b. The comparison is close qualitatively but cannot be made precisely so; however, an extended 4-box model with upper and lower equatorial boxes and separate boxes for each polar region can be shown to have a quantitatively very close correspondence to the 2D fluid model. Other equilibria break the symmetry and exhibit sinking only in one polar region; these we designate as PP (pole-to-pole). The present state of the THC in the real ocean is akin to a PP state, in that fairly symmetric surface forcing patterns give rise to a highly asymmetric circulation pattern. Notice that the TH and PP equilibria in Fig. 23 exhibit well defined pycnoclines away from high latitudes, but SA does not. This demonstrates that the THC is indeed the controlling influence on the maintenance of the pycnocline. The general regime diagrams are shown in Fig. 24, with an accompanying categorization of the types of bifurcations associated with the loss of stability of various equilibria; these are determined from many integrations of (23)-(24) to their steady state.

For larger values of a, b than those examined above, there are further bifurcations in (23)-(24) to time-varying solutions. One example of a periodic oscillation (*i.e.,* due to a Hopf bifurcation) between opposing PP states in the two different hemispheres is shown in Fig. 25. Its period is on the order of a parcel recirculation time in the PP configuration; *i.e.,* on the order of 10^3 years. A different kind of behavior is shown in Fig. 26: a PP equilibrium — associated with surface forcing patterns somewhat different from (24) — is stable under steady forcing, but it exhibits a well-

defined oscillation with local variations in the strength of the THC near the sinking regions when stochastic surface forcing is included. Thus, this oscillation is sub-critical, at least for these values of the control parameters. Its time scale is decadal, independent of the time-scale of the forcing. This makes it potentially relevant to shorter-period climate variability because the atmosphere has its own intrinsic variability that cause fluctuations in the surface buoyancy flux. In the noisy reality of nature it usually is unimportant whether an oscillation is super-critical or moderately sub-critical in any particular model configuration; it will be manifested in the solution behavior in either case.

3 Idealized 3D Models

For all of these simple models, of course, there is a need to demonstrate their relevance to the fully 3D ocean. 3D dynamics is the subject of the next section. However, we can here summarize their relevance broadly as follows: κ_v does play an important role in the maintenance of the pycnocline, although it is not true that w exhibits nearly uniform upwelling at the pycnocline base; the multiple equilibria of box and 2D models do have 3D counterparts; and there is also intrinsic variability of the 3D THC, especially on the decadal time scale. The clearest failings of these simpler THC models are their absence of geostrophic balance for the zonally averaged v, which in a 2D model requires an excessively large ν_v or ν_h value to compensate for the lack of a zonal pressure-gradient force. A 2D model also lacks a narrow DWBC because of the absence lack of zonal variation. At the least, these deficiencies are likely to cause a bias in the parameter correspondences between 2D and 3D model regimes; *e.g.,* a small diffusivity acting on a narrow current in 3D can have the same integral effect as a broad diffusivity acting on a broadly distributed current, and an approximate geostrophic balance in 3D can greatly reduce the requirement for eddy diffusion in the momentum balance.

3.1 Thermocline Theory

There is a body of theoretical studies based on the Planetary Geostrophic Equations:

$$\begin{aligned} f\hat{\mathbf{z}}\times\mathbf{u}_h &= -\boldsymbol{\nabla}\phi - \frac{g}{\rho_o}(\rho-\rho_o)\hat{\mathbf{z}} \\ \boldsymbol{\nabla}\cdot\mathbf{u} &= 0 \\ \frac{D\theta}{Dt} &= \kappa_v\partial_z^2\theta \\ \frac{DS}{Dt} &= \kappa_v\partial_z^2 S \\ \rho &= \mathcal{R}[\theta,S]\,, \end{aligned} \tag{25}$$

which implies a parcel conservation of $Q_{pg} = fb_z = fN^2$ (*cf.,* Chap. 1, Sec. 7.7). Accompanying (25) are surface boundary conditions of Ekman pumping for w and specified distributions

of T and S. In most applications κ_v is taken to be small (or even zero, where 25 is called *ideal* thermocline theory), which is appropriate in stably stratified regions but not actively convective ones. This model is proposed as relevant to the large-scale circulation below the surface boundary layer and away from western-boundary and equatorial regions, other places with strong currents or topography, and sites of deep convection. For these reasons it obviously is an incomplete model for the general circulation.

However, as stated in the review by Pedlosky (1987), "The main objective of thermocline theory is to explain the phenomenon of the strong, vertical temperature gradient in relatively shallow water (200-800 m) where the transition occurs from the ocean's surface temperature to the colder, more uniform waters of the abyss." Its implicit premise is that — while the existence of a pycnocline may fundamentally be due to the THC as a whole (*e.g.,* even the simple 1D model above requires an abyssal upwelling velocity, which also is an ingredient in the Stommel-Arons conceptual model) — its interior distribution in space arises as a consequence of hydrostacy, geostrophy (hence planetary vorticity balance), and advective tracer conservation, given the surface distributions of Ekman pumping and tracers.

Even the simplified dynamics of the nonlinear equations in (25) gives rise to rather complex and elegant mathematical analyses. The solutions do have some qualitative features as observed, *viz.,* , the general deepening of the thermocline moving from the equator into the subtropical gyre with subsequent rising again into the subpolar gyre and the general shallowing of the pycnocline approaching the eastern boundary. Of course, to a large extent these features are simply consequences of the pattern of Ekman pumping and geostrophic balance, given the confinement of the Sverdrup circulation in and above the pycnocline. This latter feature is therefore the principal success of thermocline theory, *viz.,* some of its solutions have this feature.

My principal criticism of (25) is that it neglects the role of mesoscale eddy fluxes of T and S (*e.g.,* as parameterized by isopycnal mixing and eddy-induced transport-velocity advection) that are likely to be significant in modifying the implied conservations of T, S, and Q_{pg} along mean-flow trajectories when $\kappa_v \rightarrow 0$ in (25). There is a sharp contrast between the quasigeostrophic wind-gyre solutions (Chap. 3) — which assumes the mean vertical stratification profile (*i.e.,* a substantial part of the thermocline shape) and has the dilemma of surface confinement in the absence of mesoscale-eddy form stresses — and the Planetary-Geostrophic ideal thermocline theory — which assumes the surface T and S distributions (*i.e.,* also a substantial part of the thermocline shape, but a different part) and determines their subsurface distribution in the absence of eddy effects. Undoubtedly there is some degree of validity in from each of these theories. It has long seemed to me worthwhile to extend the analytic thermocline theory by including parameterized mesoscale effects, but as yet no one has done this.

The equations in (25) may be extended by adding drag or viscous diffusion to the horizontal momentum equations, in which case the model is capable of representing diffusive western boundary layers and thus the linear momentum dynamics for wind gyres in closed basins. Colin de Verdiere (1976) and Samelson and Vallis (1997) give examples of basin-scale solutions in such extended Planetary Geostrophic models.

3.2 The Ventilated Thermocline

Another influential theoretical perspective is the so-called *ventilated thermocline*. It is a combined wind- and buoyancy model that is particularly relevant to the eastern part of the subtropical gyres (*i.e.,* away from the western boundary current, its strong offshore extension, and the recirculation zone). It also makes use of the Planetary Geostrophic equations. Because the theory is mathematically rather elaborate, it is not presented here, but it is extensively discussed in Pedlosky (1996).

3.3 Sector Models

The simplest relevant 3D THC model is one in a basin shaped either as a rectangular box or as a spherical-shell sector bounded by lines of constant longitude (as in Fig. 17). Since there is more interest in the THC on the planetary scale, the latter choice has been made more often. Furthermore, the common practice has been to use an OGCM in sector THC studies, even though simpler alternatives for the equation of state and for the various SGS parameterizations might allow a more distilled depiction of the essential dynamics. One essential aspect of the parameterizations, however, is use of a nonlinear vertical eddy diffusivity for tracers (and also for momentum if one is being consistent) with the following property:

$$\begin{aligned} \kappa_v &= \kappa_1 \quad \text{if } b_z < 0 \\ &= \kappa_0 \quad \text{if } b_z > 0\,, \end{aligned} \tag{26}$$

where $\kappa_1 \gg \kappa_0 \geq 0$. The rationale for this behavior is the greater mixing efficiency of convection in gravitationally unstable situations and the necessity for wholly parameterizing convective effects in the hydrostatic Primitive Equations that are the basis for almost all OGCMs. Sometimes (26) is represented in a more differentiable form with κ_v expressed as a continuous function of the stratification b_z if not more fundamentally of the Richardson number,

$$Ri \;=\; \frac{b_z}{(\mathbf{u}_z)^2}\,.$$

One of the earliest uses of a sector model is by Bryan (1986). It shows that steady, stable pole-to-pole circulations can arise even with equatorially symmetric forcing and that multiple equilibria do indeed exist in 3D, just as in the box and 2D models.

More extensive uses of sector models have addressed the intrinsic variability of the THC (Weaver et al., 1993) even with steady surface boundary conditions. This phenomenon is not well represented in any of the even simpler models. Yet, because of the central role of THC meridional fluxes in maintaining climatic heat balance, THC oscillations are obviously of potentially great relevance to natural climate variability. Surface boundary conditions that permit such oscillations in ocean-only, coarse-resolution OGCMs can be either of the mixed type (*i.e.,* thermal relaxation and specified S flux) or the flux type with both T and S fluxes specified. Of course, neither type

represents the true, albeit still poorly known, ocean-atmosphere feedback that occurs in the presence of THC variability, but the mixed type seems somewhat more plausible, since local thermal feedbacks in air-sea fluxes are strong, while local water feedbacks are virtually non-existent. With mixed boundary conditions plus climatological wind stress, the spontaneous oscillations fall into two classes:

1. Flushing oscillations with periods of millennia, in which long intervals of slow diffusive evolution are punctuated by abrupt overturning events at high-latitudes.

2. Decadal oscillations with fluctuations in both the amplitude of the meridional overturning circulation and lateral advection of T and S anomalies primarily by the subpolar gyre.

For different model parameters and surface flux patterns, these oscillations may or may not appear. On the other hand, with broad-band stochastic buoyancy forcing superimposed on the mean fluxes or with coupling to even an idealized atmospheric model with its own intrinsic variability (*i.e.,* weather noise) (Saravanan et al., 2000), it appears to be quite common for at least the decadal THC fluctuations to be manifest (Fig. 27).

Decadal oscillations are also found with specified T and S flux boundary conditions, although the associated spatial patterns are rather different. Recent studies by Arzel et al. (2006) and Molemaker and McWilliams (2006) indicate that the underlying dynamical behaviors for decadal oscillations of the thermohaline circulation are fundamentally different with mixed and flux boundary conditions. For example, Fig. 28 shows bifurcation diagrams for these two ways of posing the problem as a function of the overall buoyancy forcing strength. The latter is expressed in terms of a Rayleigh number,

$$Ra \;=\; \frac{\mathcal{B}H^3}{\nu_e \kappa_e}\,,$$

where $\mathcal{B}$ is the surface buoyancy flux magnitude (either separately for heat and freshwater, or for their combination), H is the domain depth, and ν_e and κ_e are the eddy viscosity and diffusivity. For small Ra there is a unique steady solution with either type of boundary condition. With flux boundary conditions, increasing Ra leads to a simple Hopf bifurcation that is a linear baroclinic instability of the mean circulation, and it subsequently equilibrates as a periodic limit-cycle oscillation. However, for mixed boundary conditions, multiple steady-state circulations occur for larger Ra values, and a periodic oscillation emerges as a global bifurcation (*i.e.,* not associated with the linear instability of a steady circulation). At present it is uncertain which of these mechanisms for spontaneous decadal thermohaline variability is more relevant to climate variability.

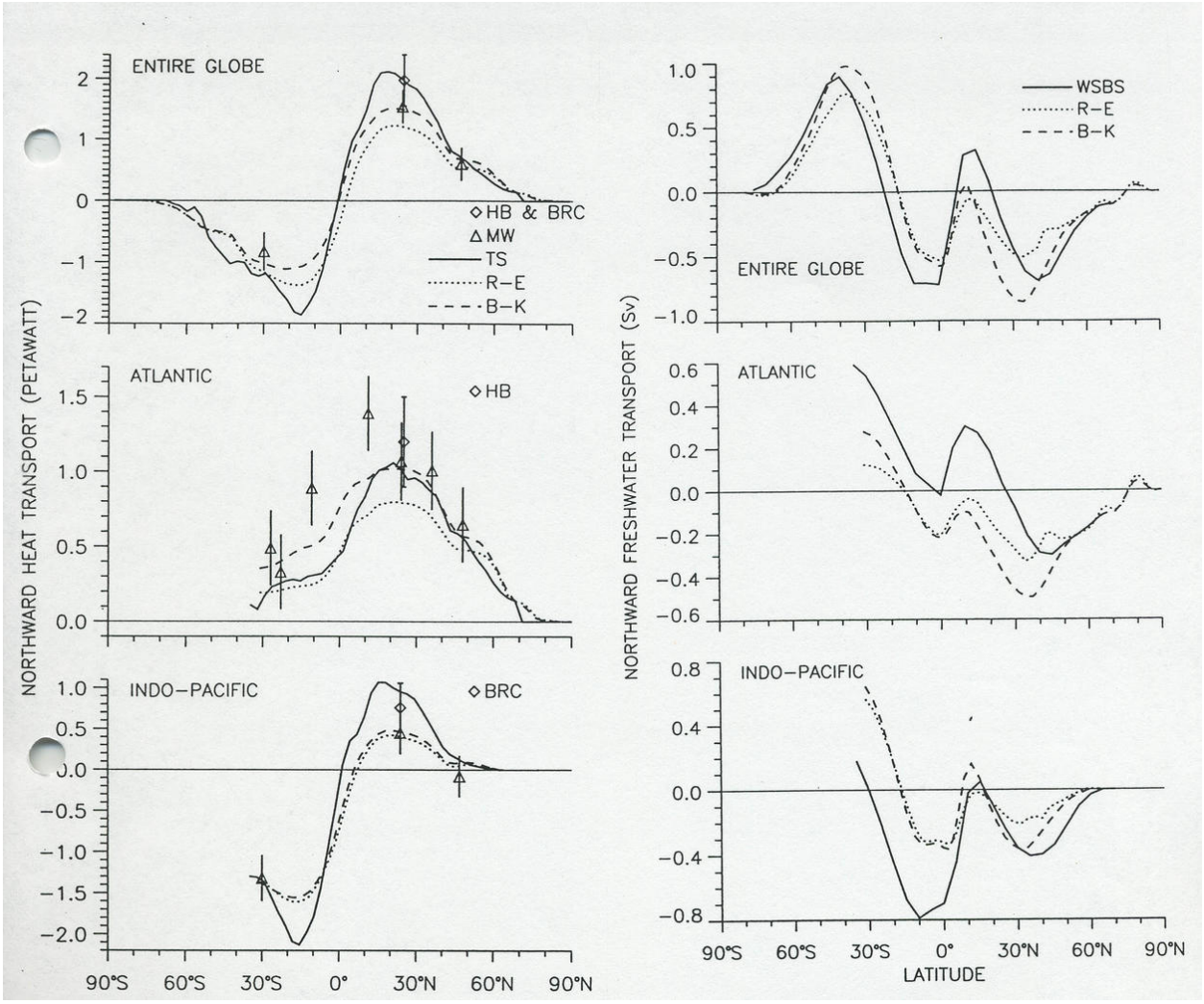

Figure 1: Annual- and zonal-mean heat and water transports from both observations and OGCM solutions (*i.e.,* R-E and B-K) (Large et al., 1997).

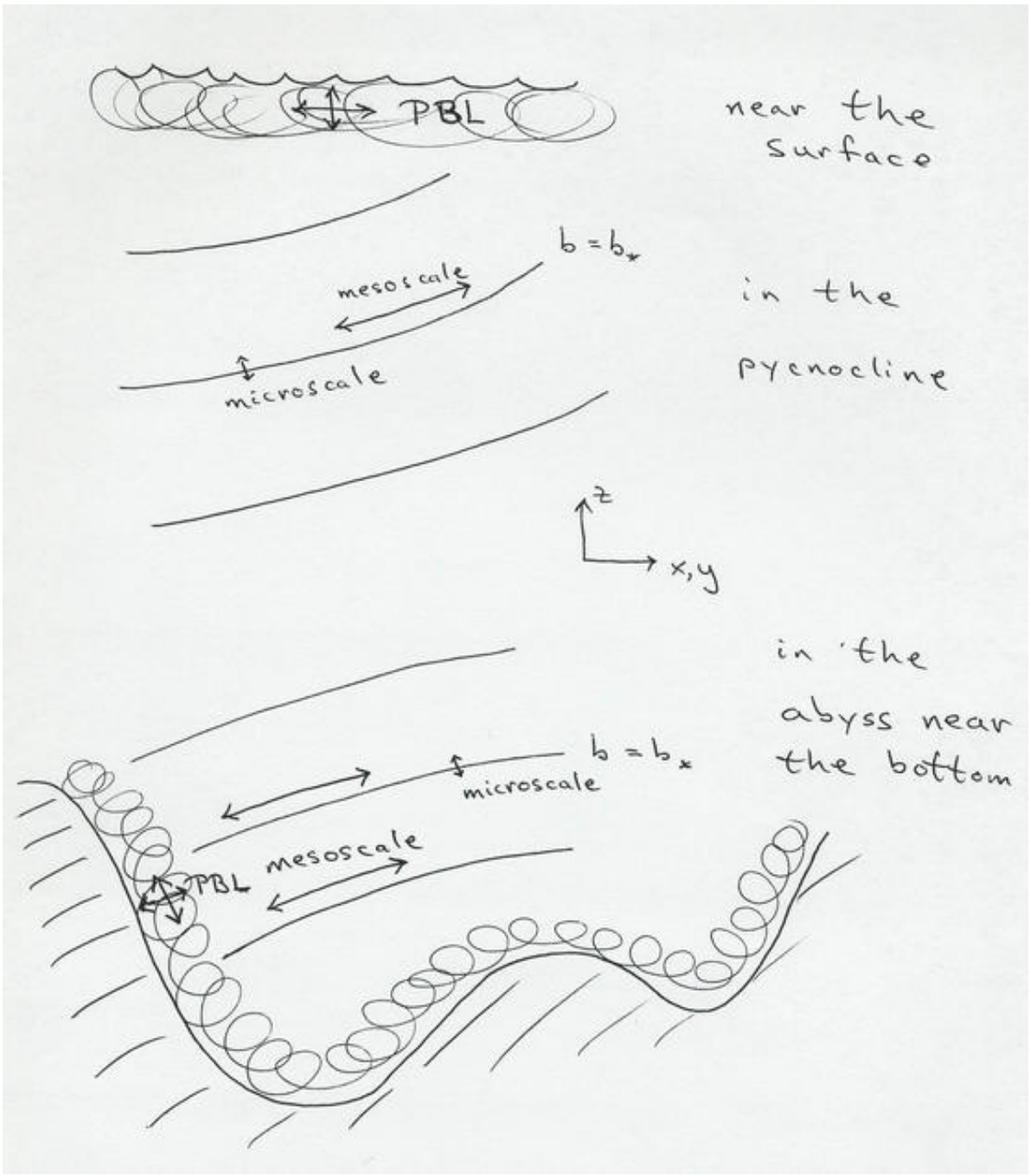

Figure 2: Schema of diapycnal mixing pathways.

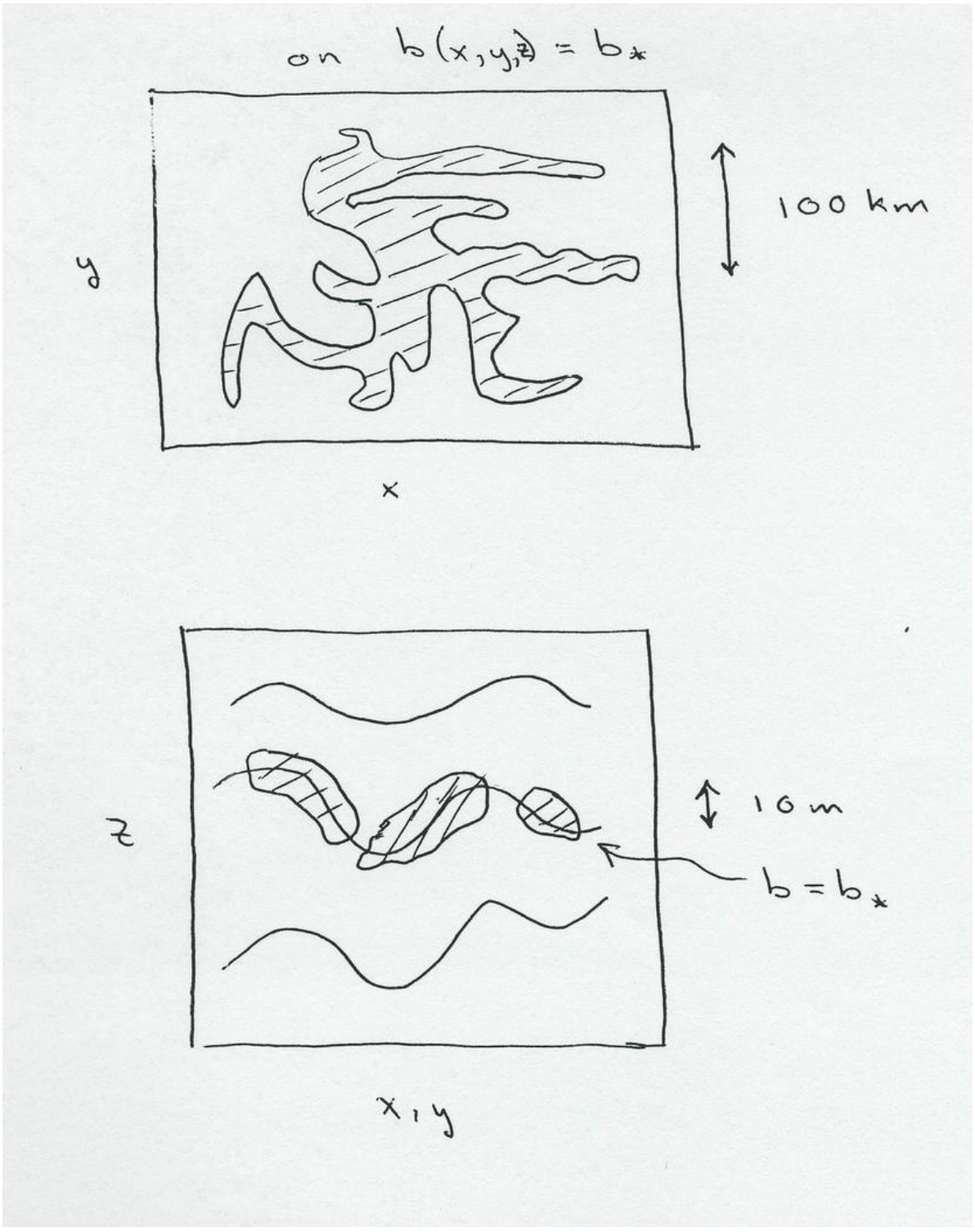

Figure 3: Schematic dye distributions in a purposeful tracer release experiment at a time approximately six months after being released at a single point.

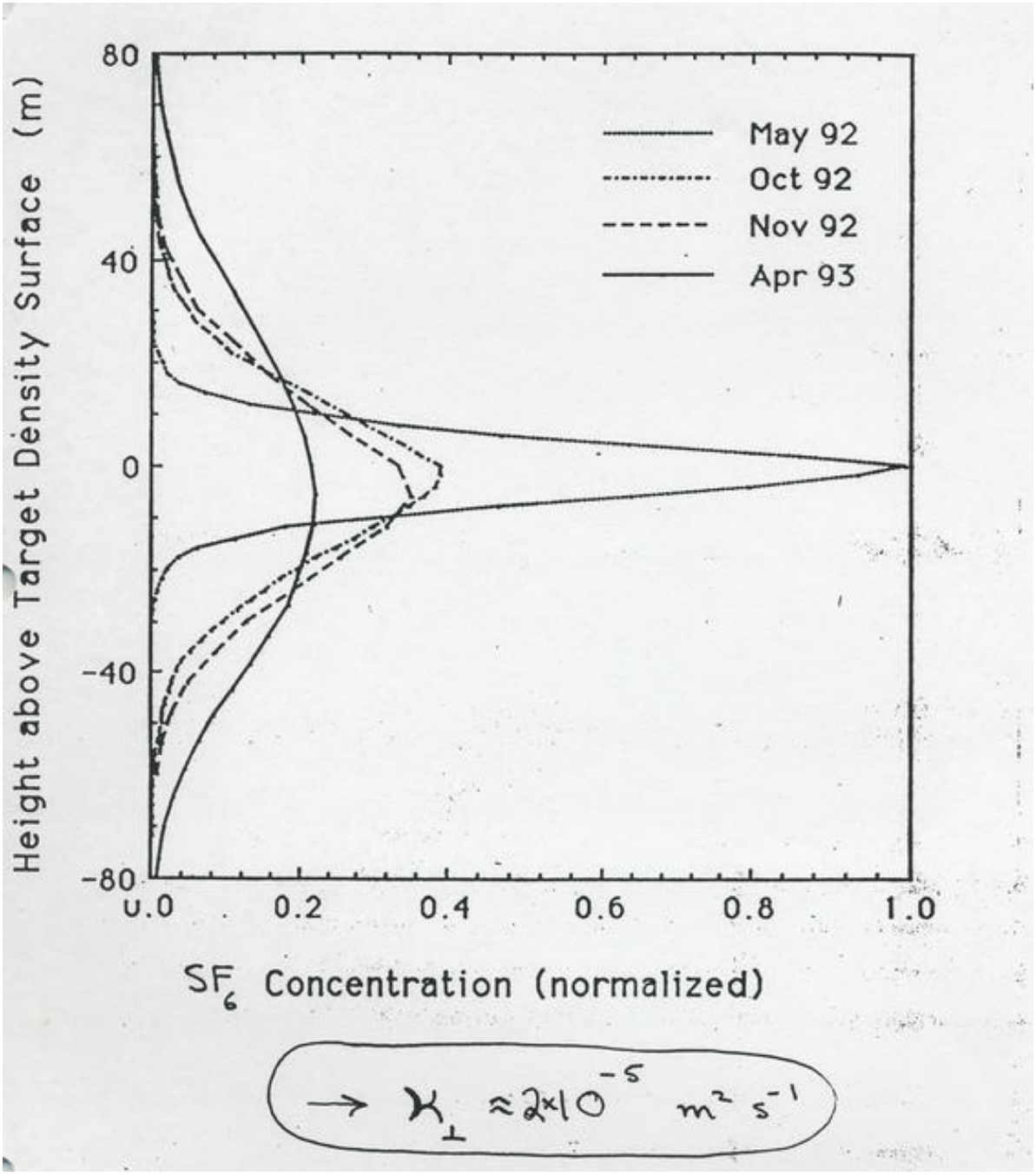

Figure 4: Diagnosed vertical eddy diffusivity, averaged horizontally, from the subtropical North Atlantic Tracer Release Experiment (TRE) (Ledwell et al., 1993).

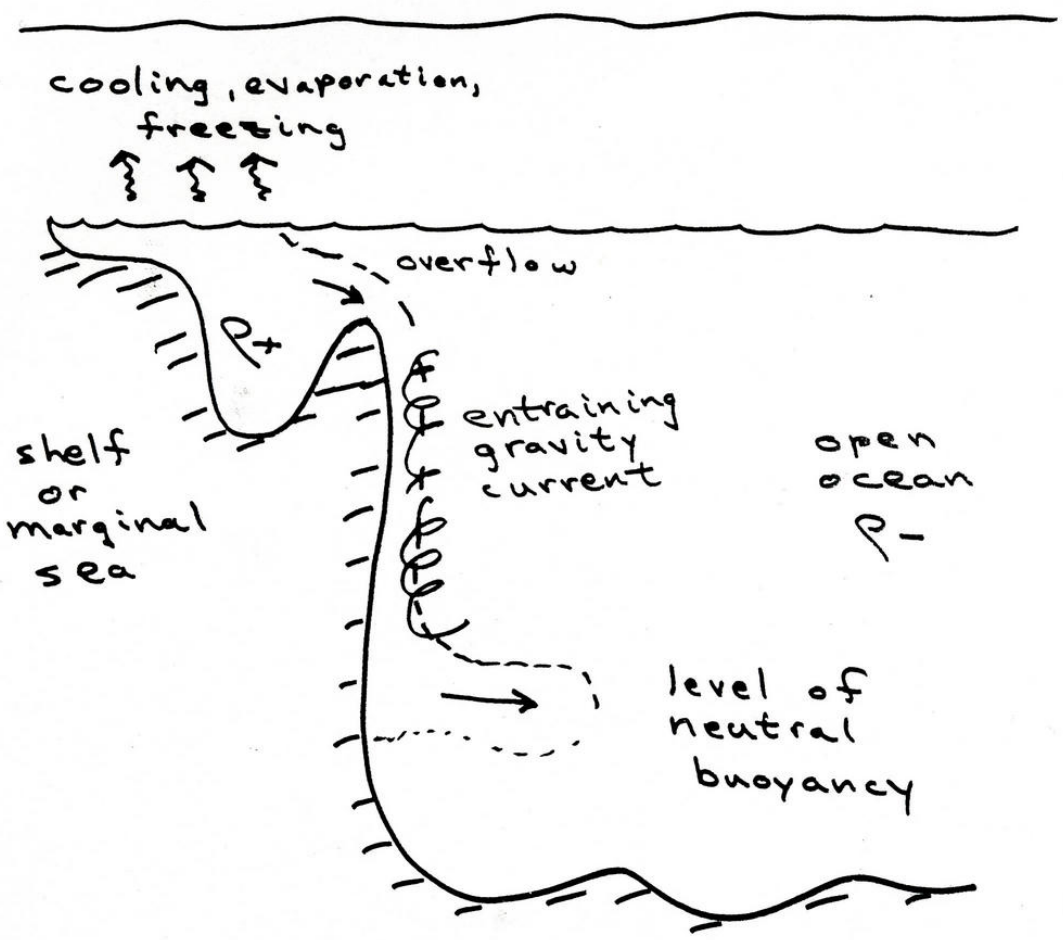

Figure 5: Schetch of water-mass renewal processes in gravity currents (*e.g.,* Greenland overflow, Mediterranean outflow, and Weddell shelf.

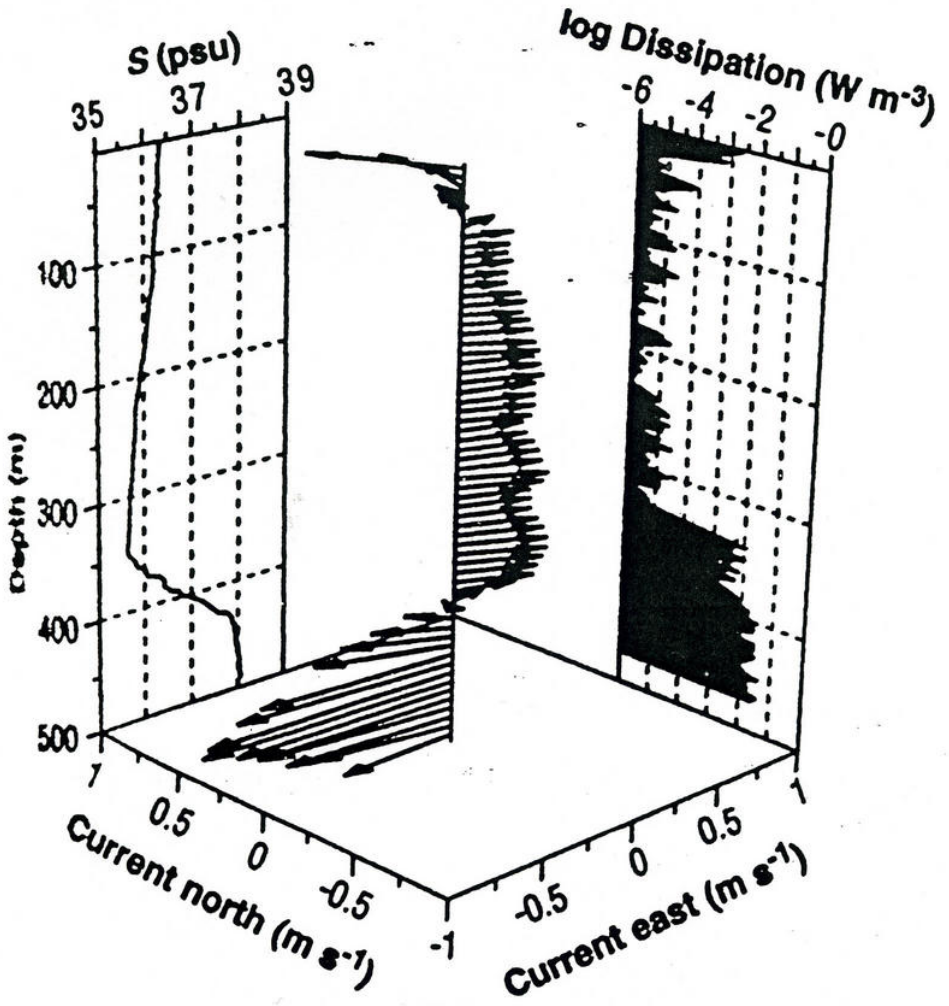

Figure 6: A profile of current and salinity and a profile of dissipation rate adjacent to the bottom within the Mediterranean Outflow in the North Atlantic (Price et al., 1993).

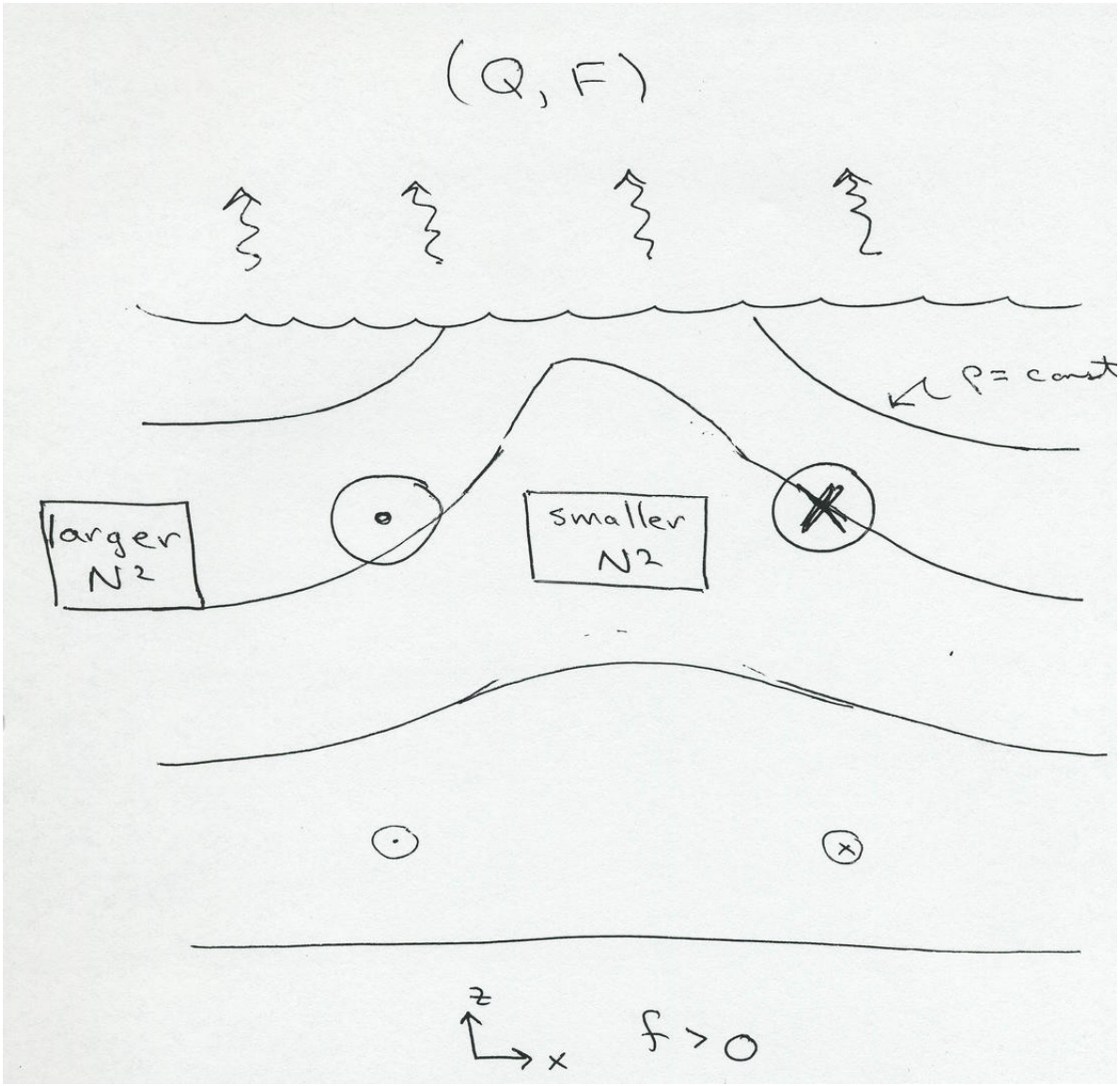

Figure 7: Schetch of a cyclonic preconditioning circulation that induces weak stratification in its center, which is more readily invaded by deep convection induced by negative surface buoyancy forcing with a larger spatial scale.

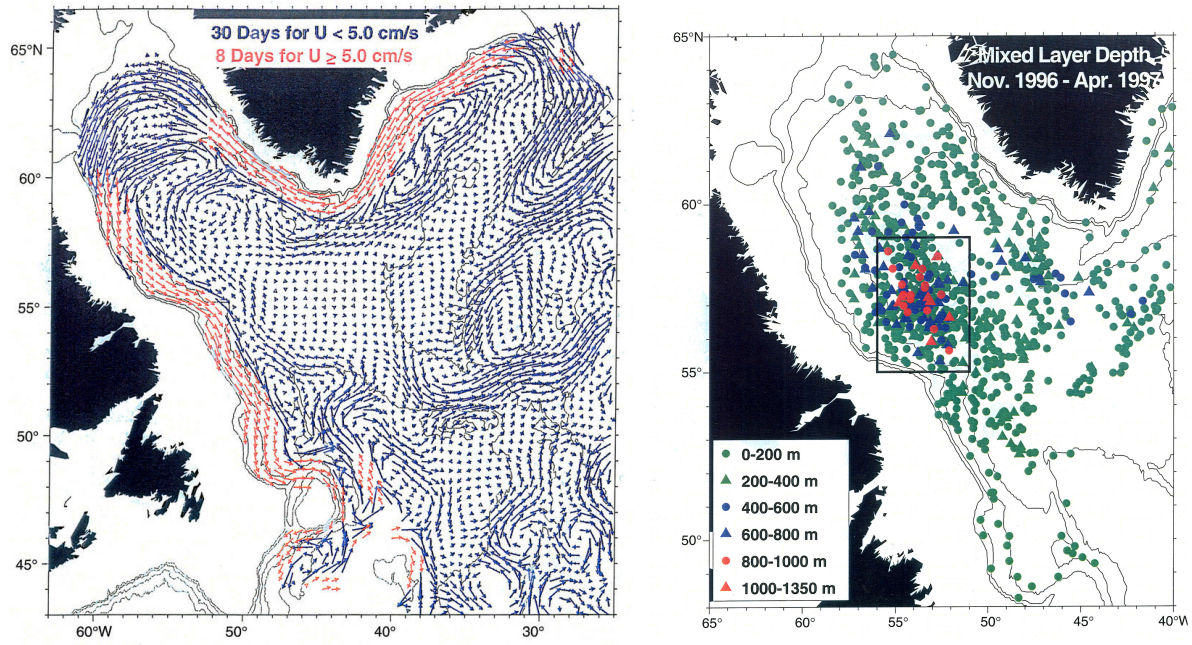

Figure 8: (Left) mean circulation of the Labrador Sea and Irminger Basin at 700 m depth. (Right) Mixed layer depths in the Labrador Sea during winter 1996-97. Measurements were made with profiling floats (Lavender et al., 2002).

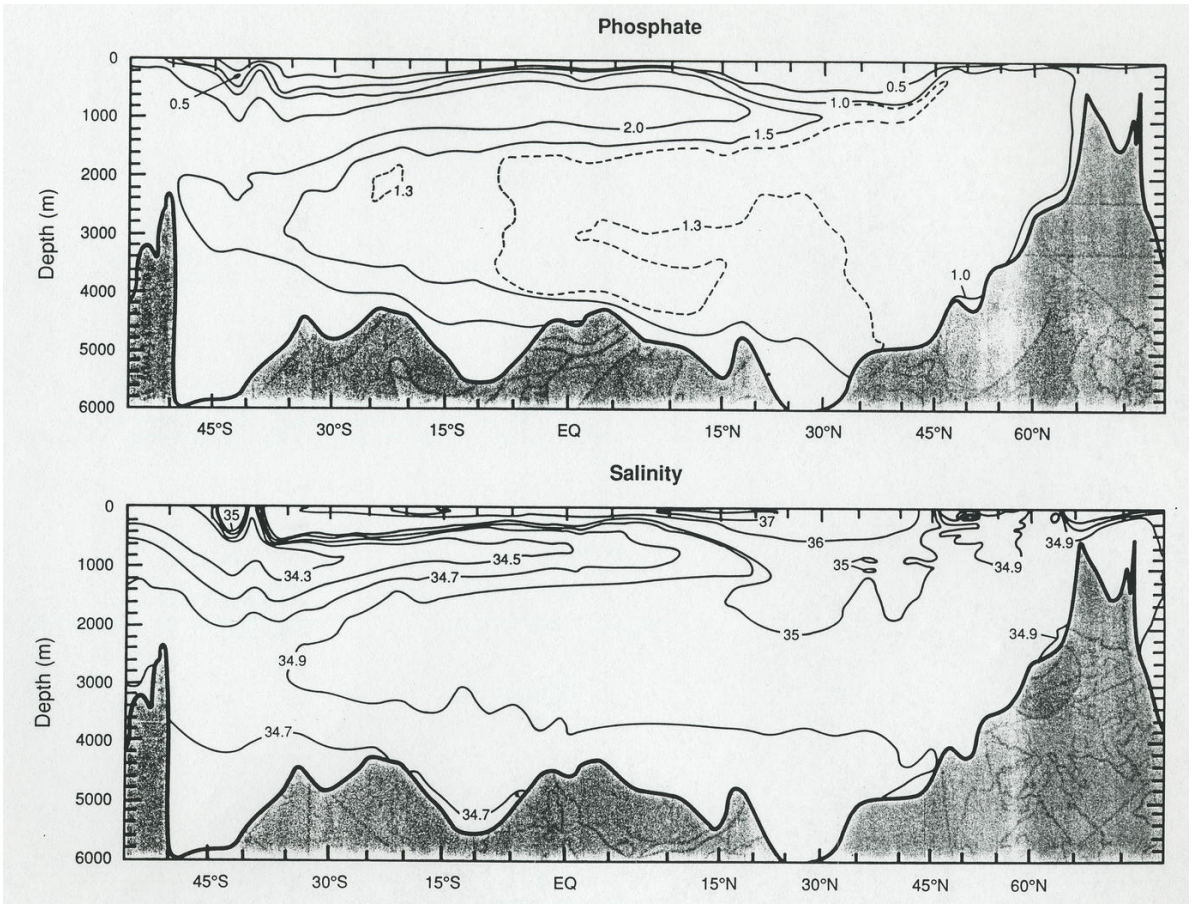

Figure 9: Phosphate and S along a meridional section in the Atlantic (Niiler, 1992).

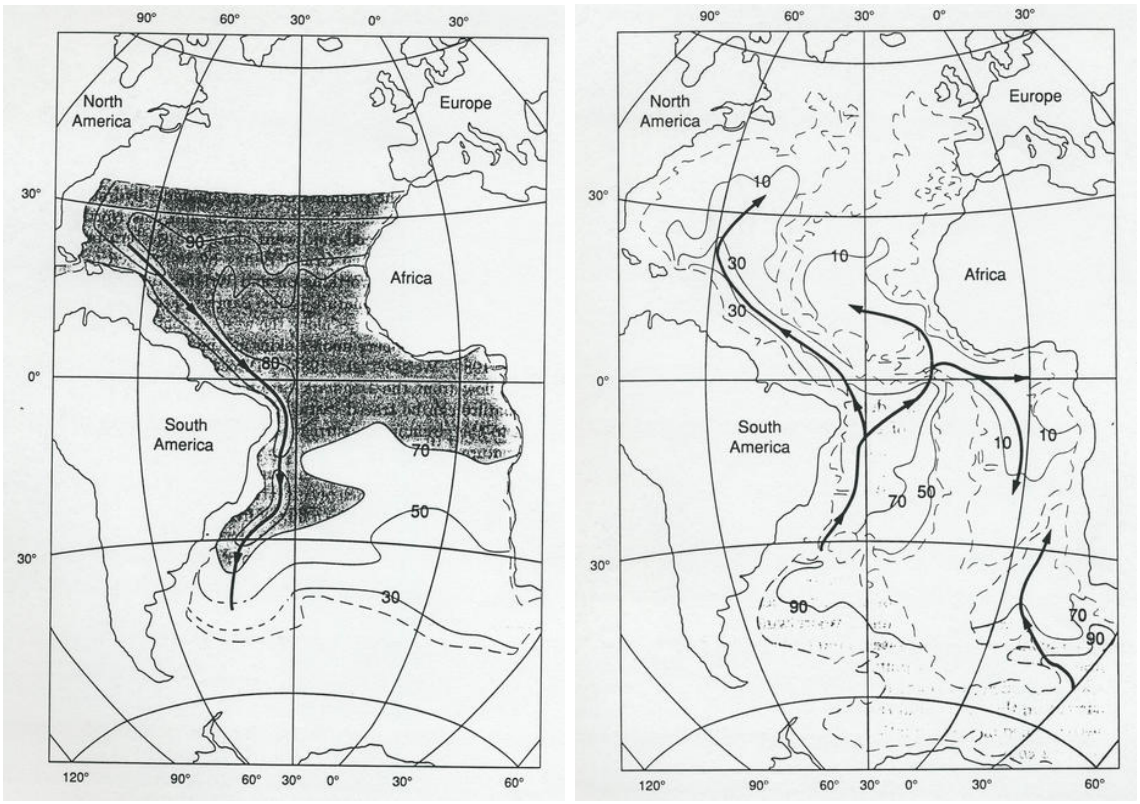

Figure 10: Spreading of NADW (top) and AABW (bottom) in the Atlantic, expressed as percentages of pure source water (Niiler, 1992).

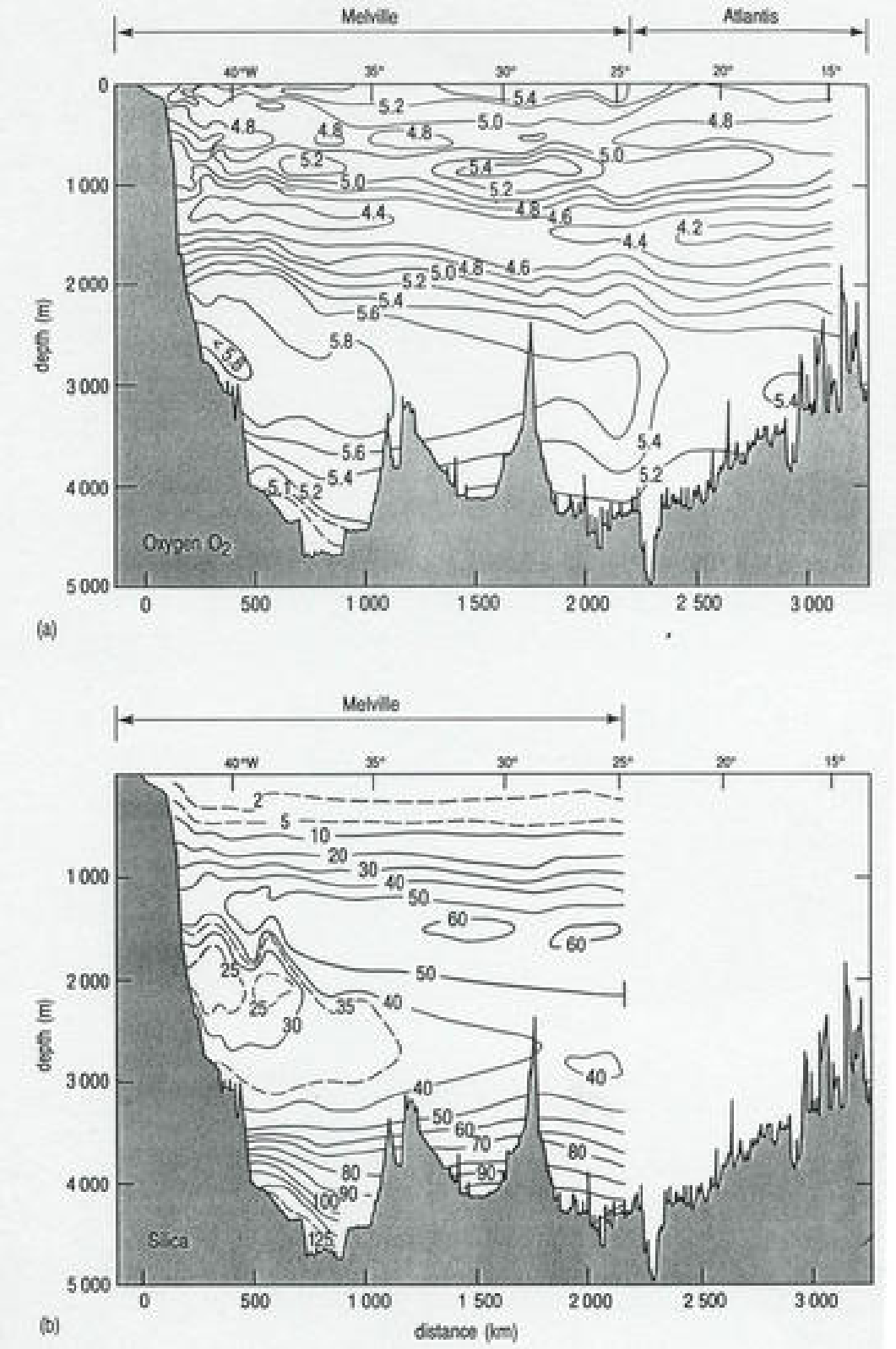

Figure 11: O_2 (top) and silica (bottom) along a zonal section in the South Atlantic.

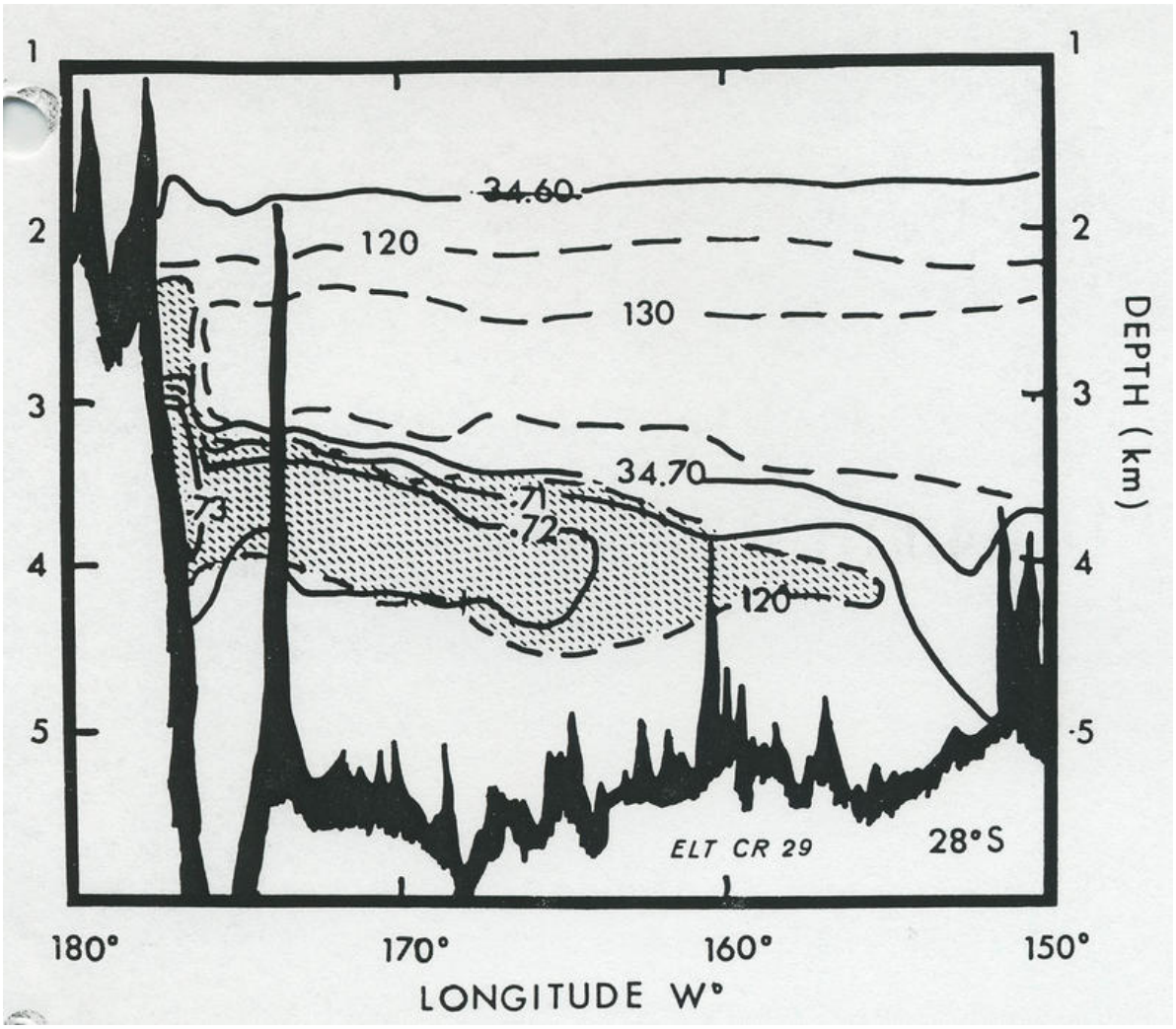

Figure 12: S (solid contours) and silicate (dashed) along a zonal section in the South Pacific (Gordon, 1975).

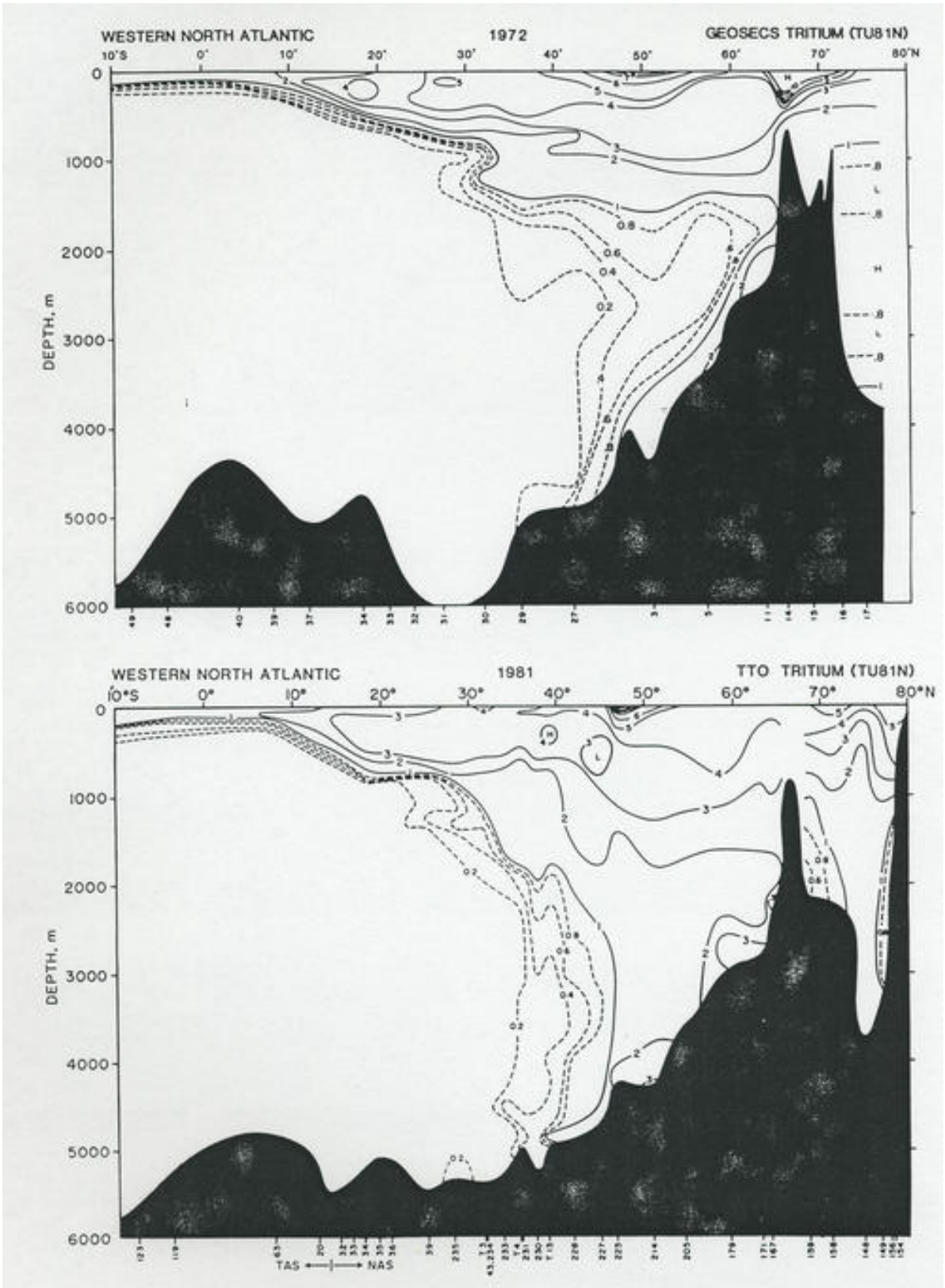

Figure 13: Tritium along a meridional section in the North Atlantic in 1972 and 1981 (Östlund and Rooth, 1990).

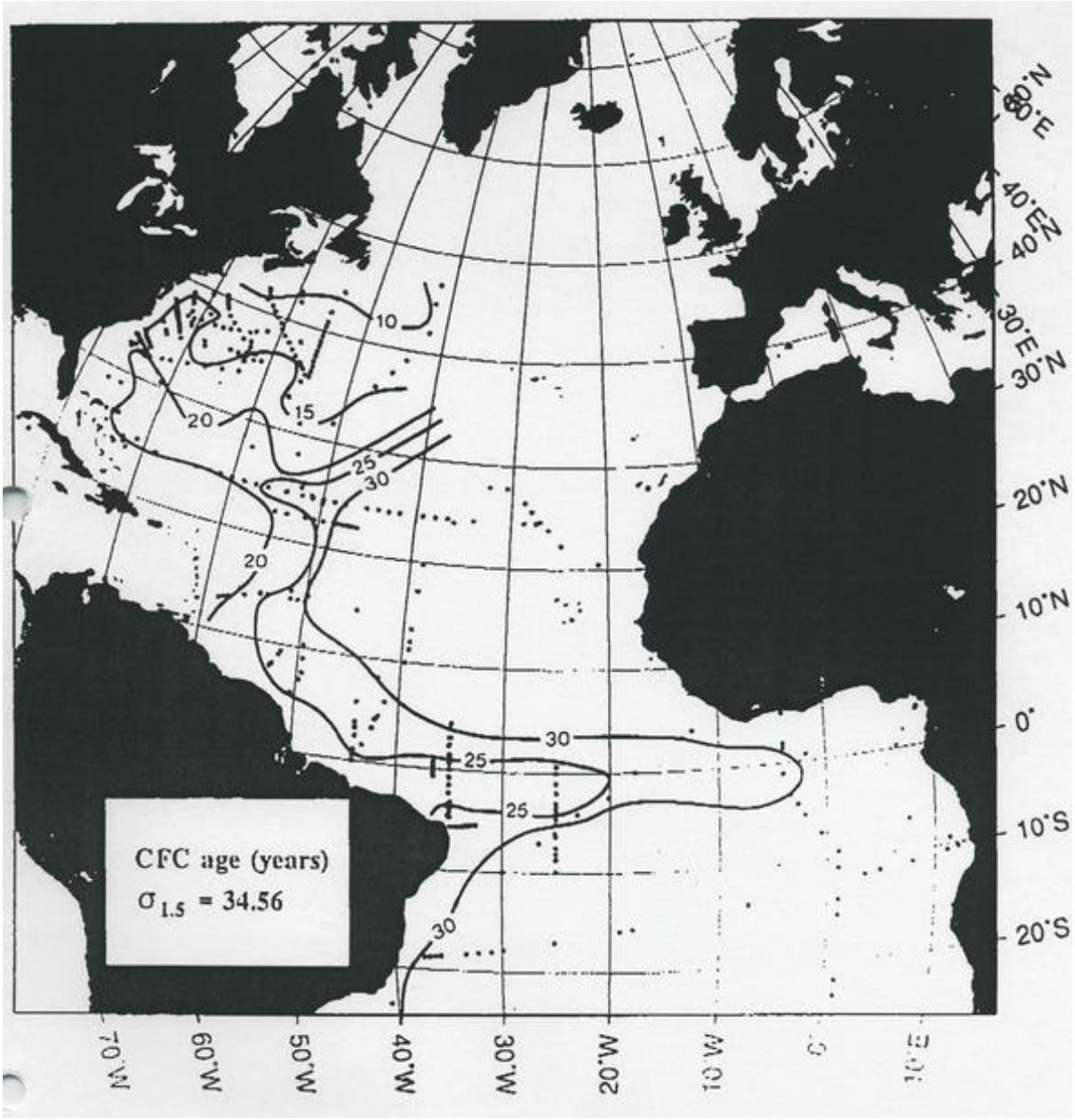

Figure 14: Distribution of time since exposure to the atmosphere (*i.e.,* age) based on Freons on a mid-level isopycnal surface in the Atlantic (Smethie and Fine, 2001).

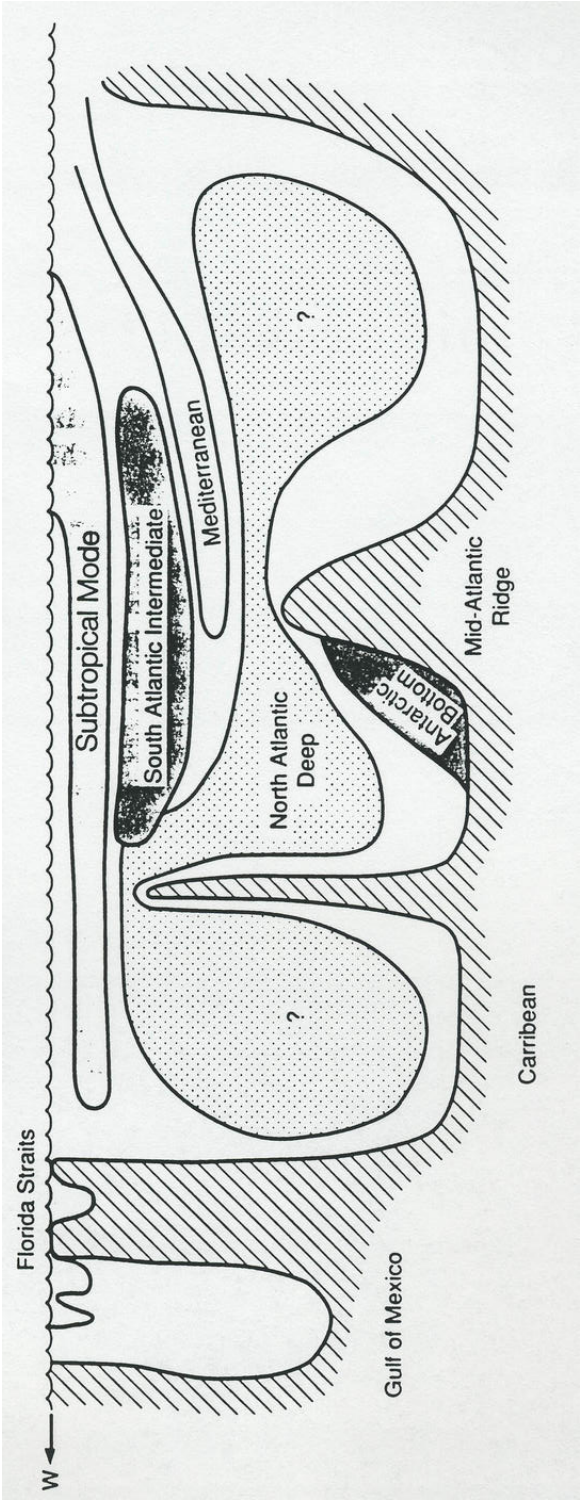

Figure 15: Schema of water masses along a zonal section at 25^o N in the North Atlantic (Niiler, 1992).

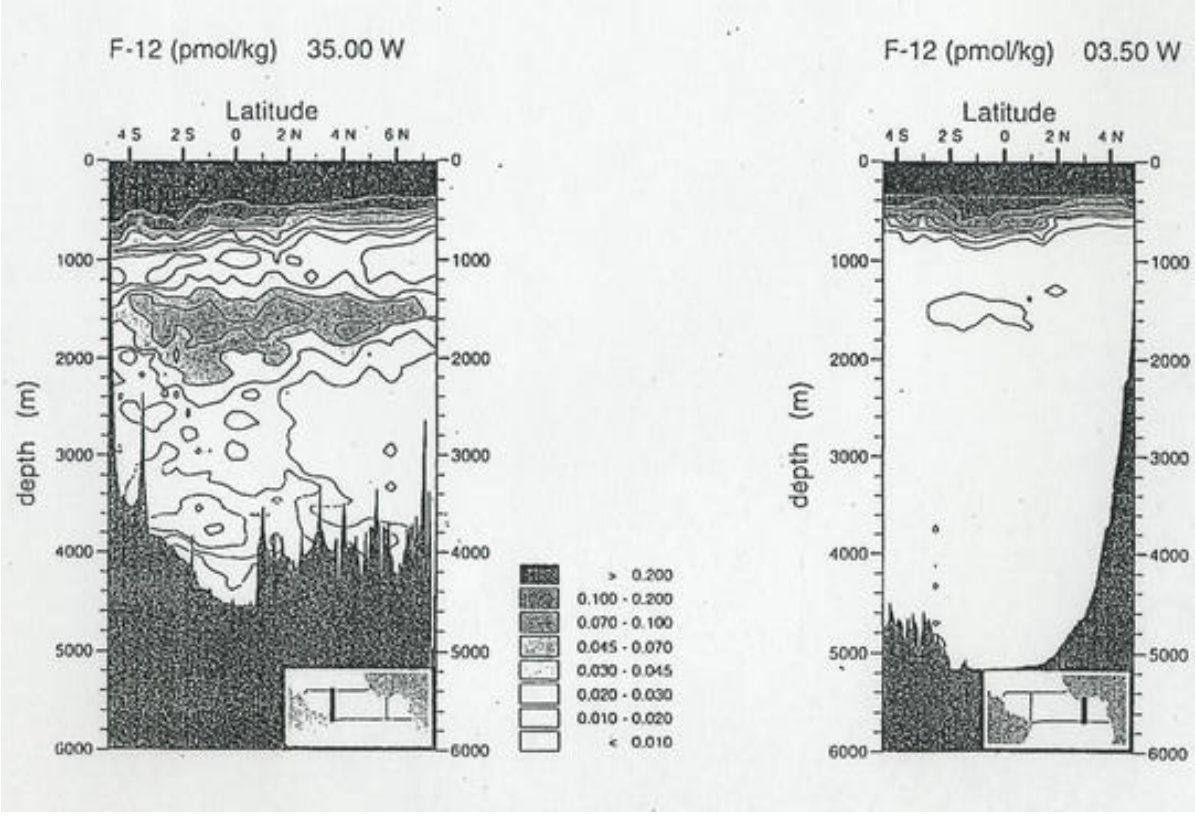

Figure 16: Freon concentrations along two meridional sections across the equator in the Atlantic.

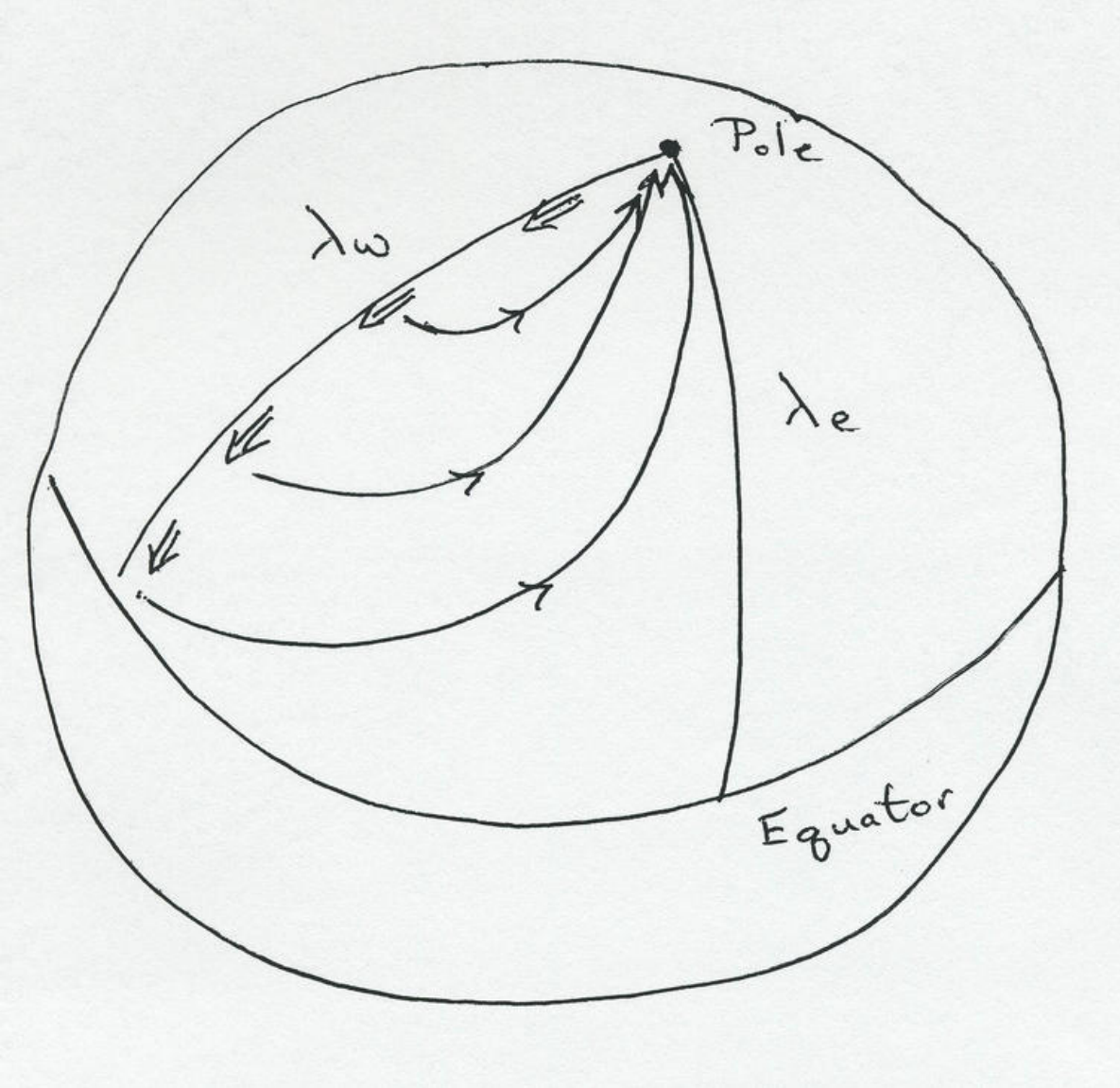

Figure 17: Stommel-Arons circulation for a hemispheric sector with a source at the North Pole.

Figure 18: Stommel-Arons circulation for the global ocean assuming two sources in the North and South Atlantic (Veronis, 1981).

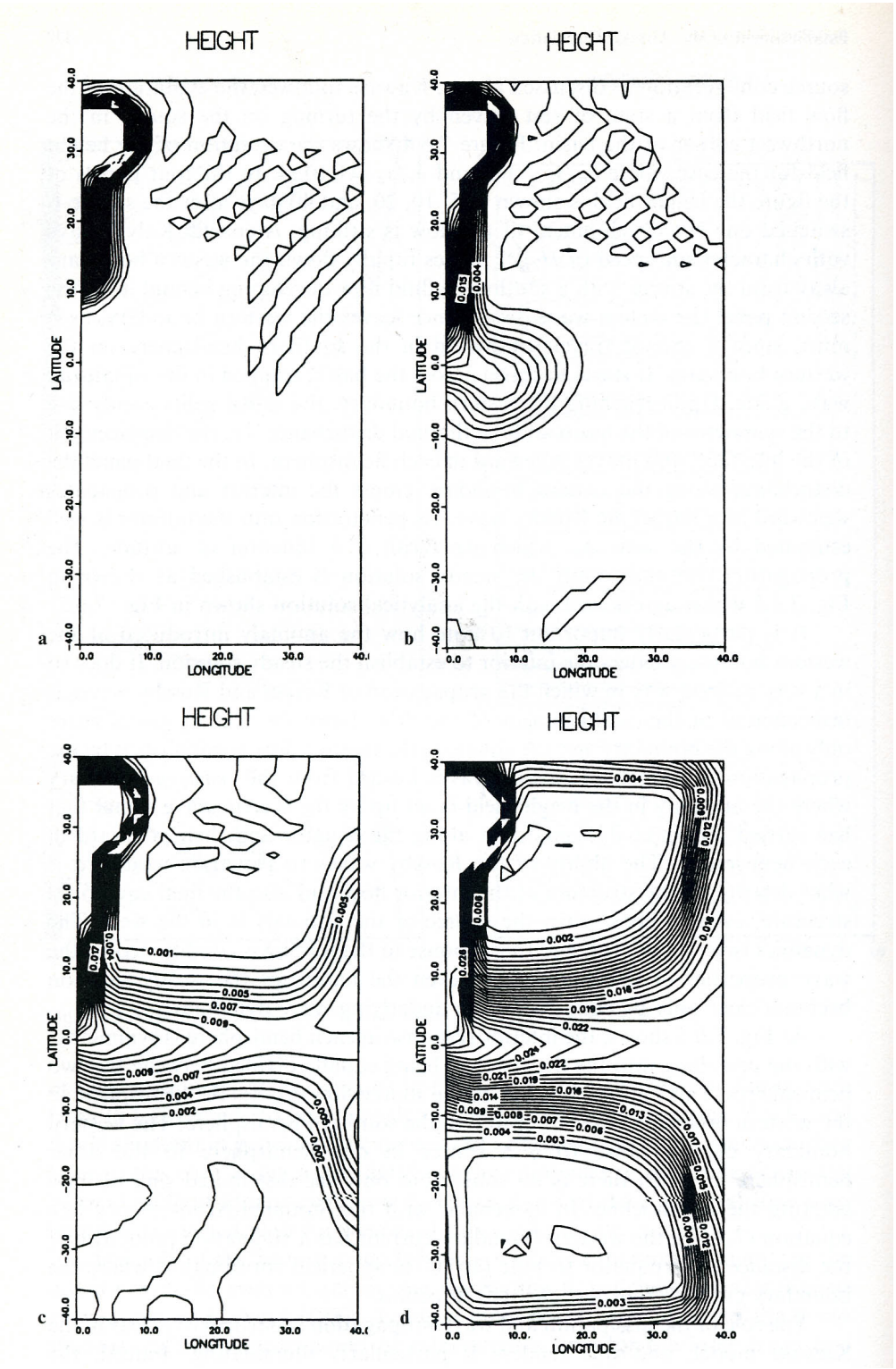

Figure 19: Establishment of the dynamic height anomaly from a state of rest in response to a mass source in the northwest corner of the basin after 5, 10, 20, and 40 days (Kawasi, 1987).

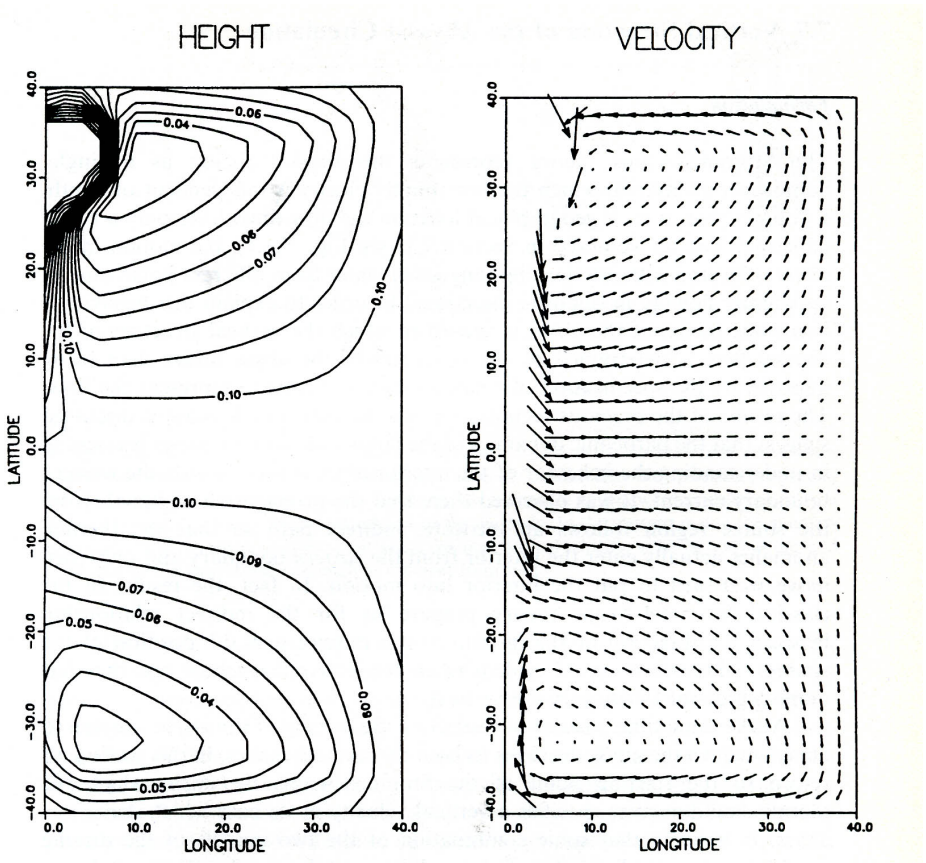

Figure 20: Final steady-state dynamic height and circulation at day 200 for the problem in Fig. 19 (Kawasi, 1987).

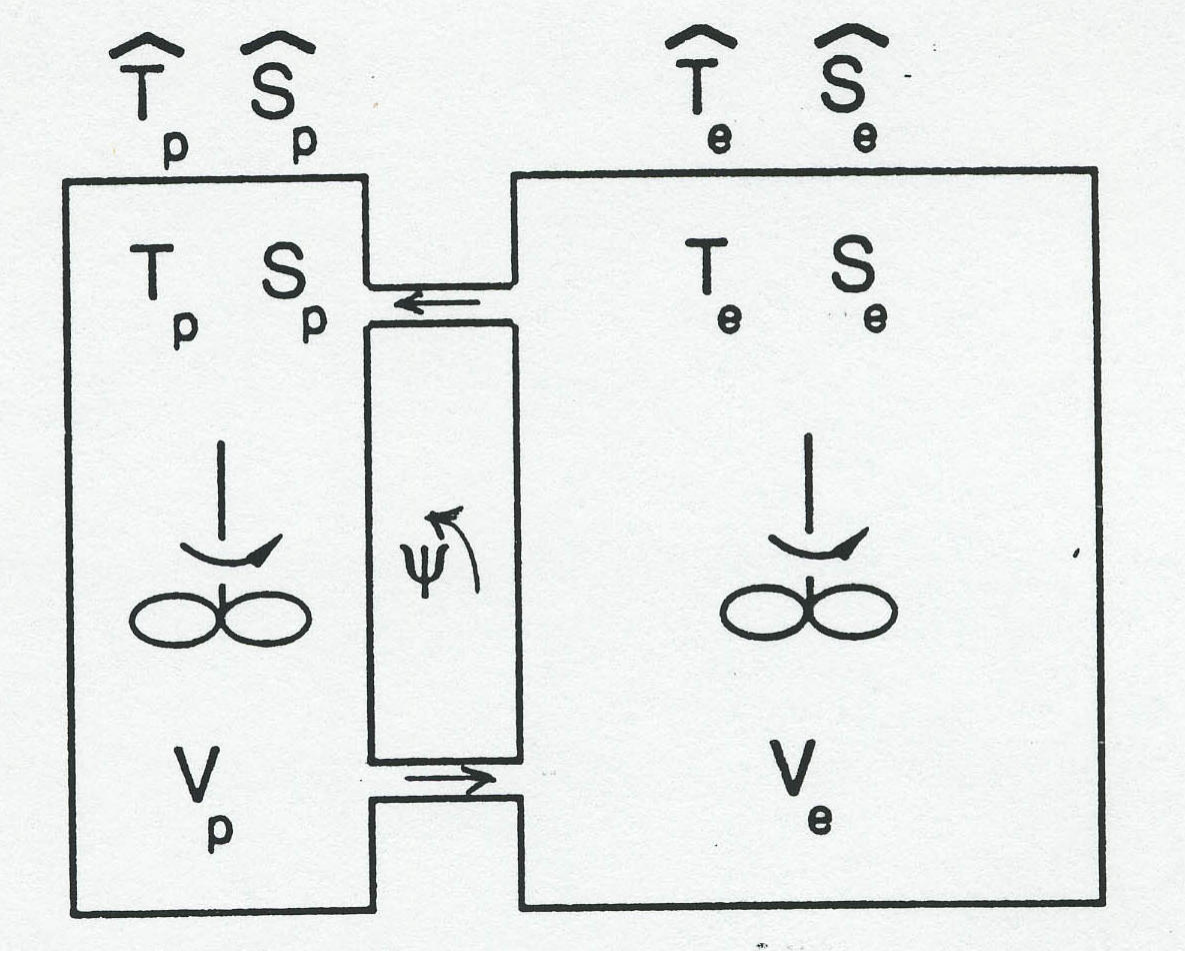

Figure 21: Configuration for a two-box model (Stommel, 1961).

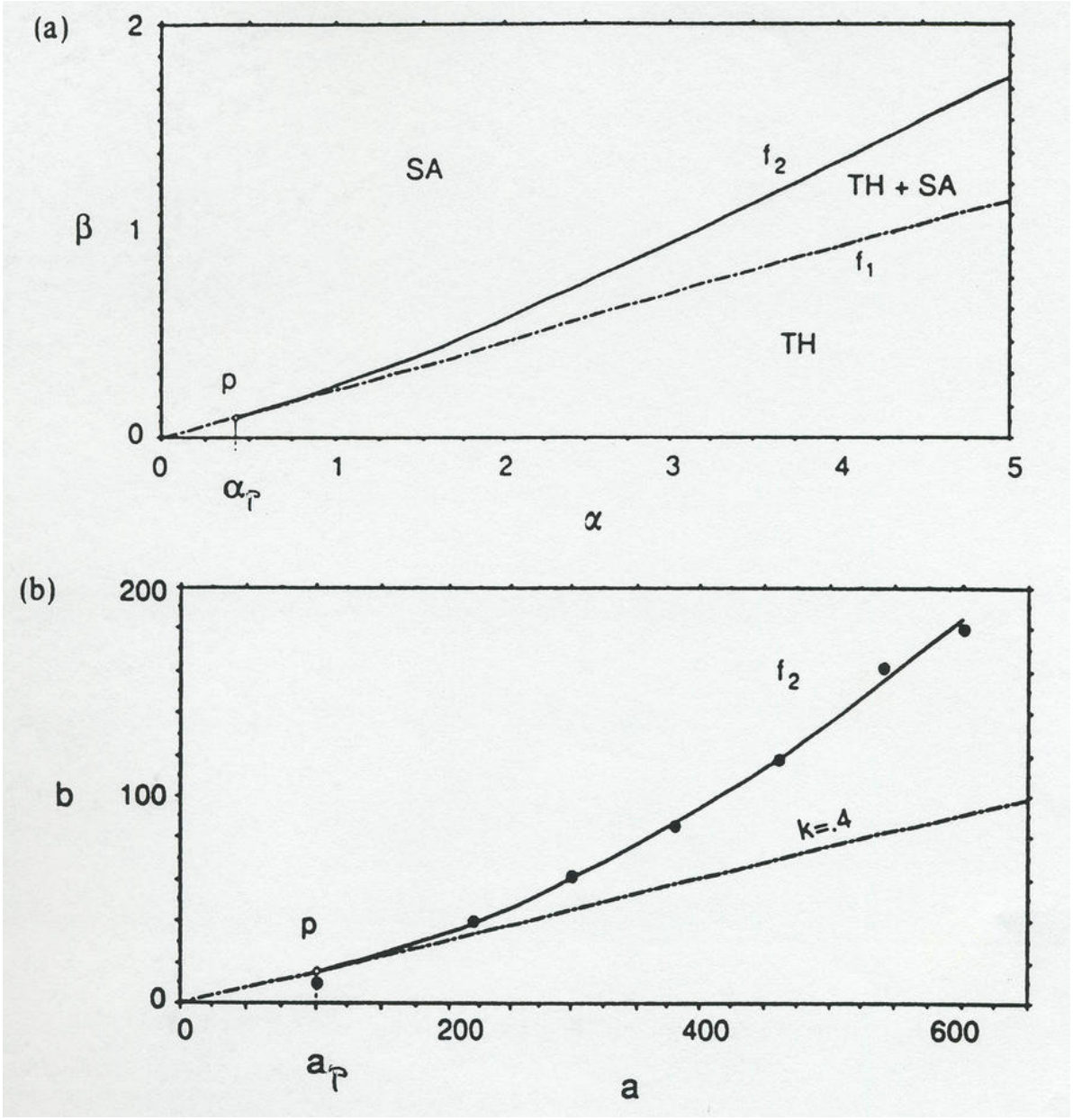

Figure 22: Bifurcation diagrams (*a.k.a.* catastrophe structure) for two-box model for two different values of ξ (Thual and McWilliams, 1992).

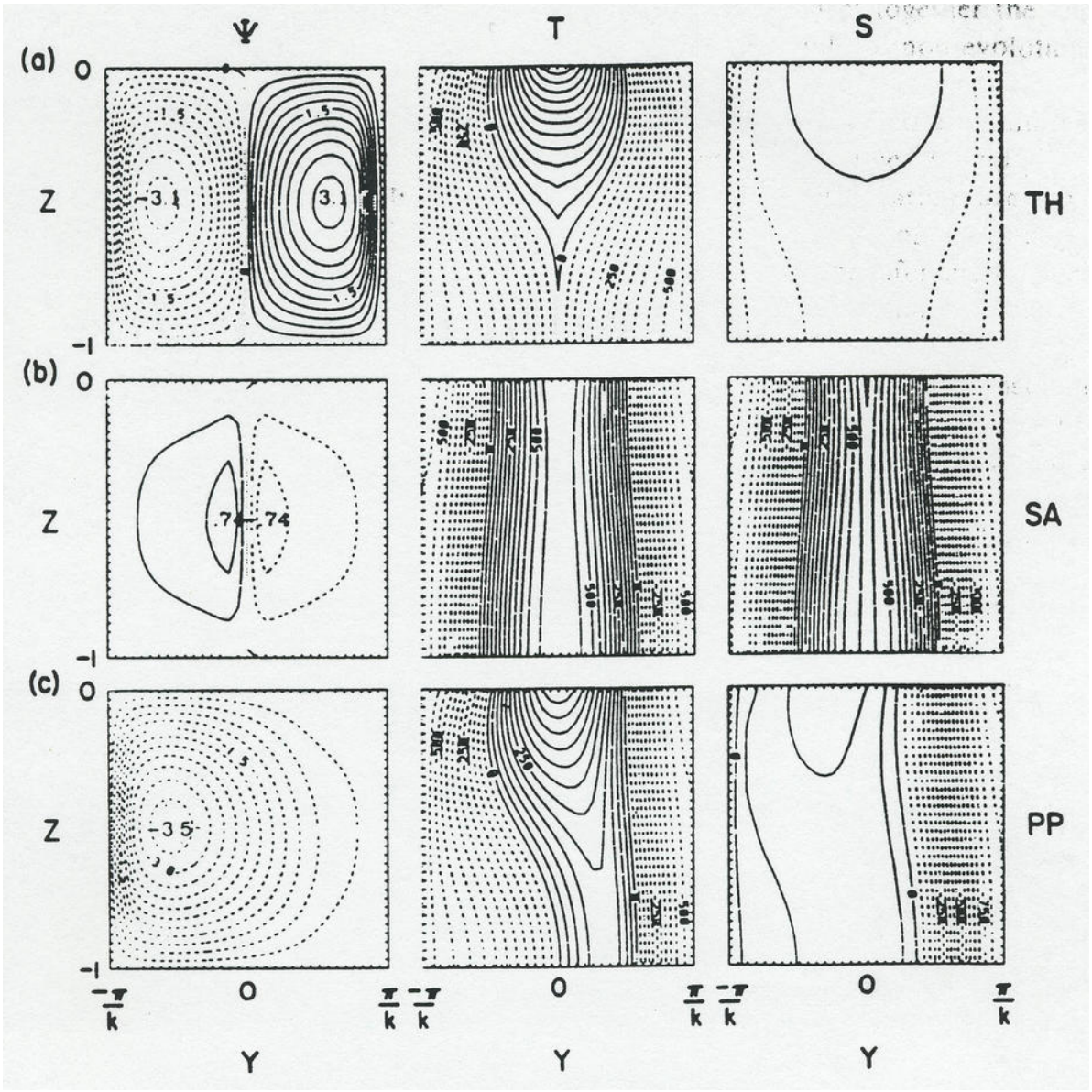

Figure 23: Multiple steady states for a 2D fluid model (Thual and McWilliams, 1992).

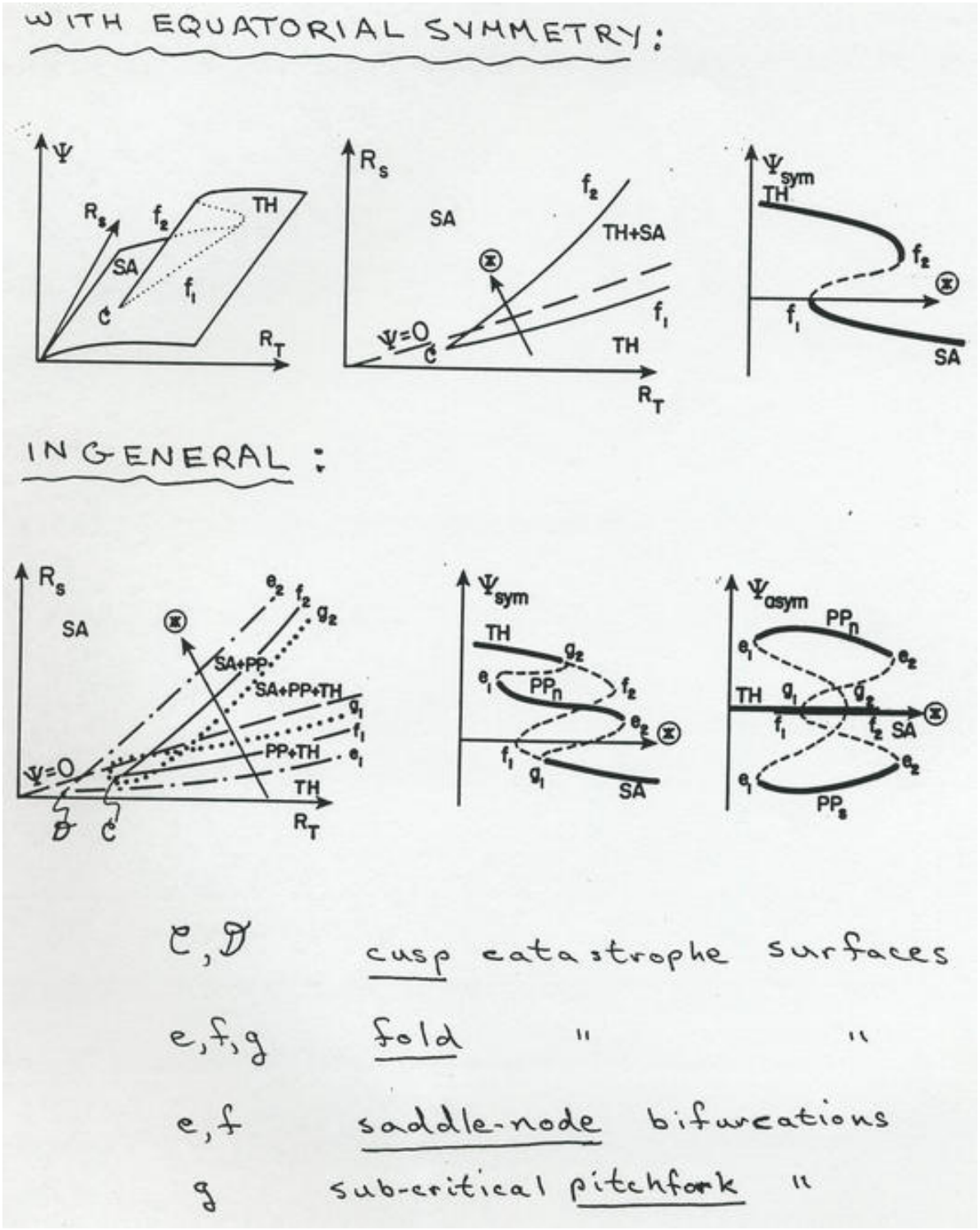

Figure 24: Bifurcation diagram (*a.k.a.* catastrophe structure) for the steady states of a 2D fluid model (Thual and McWilliams, 1992).

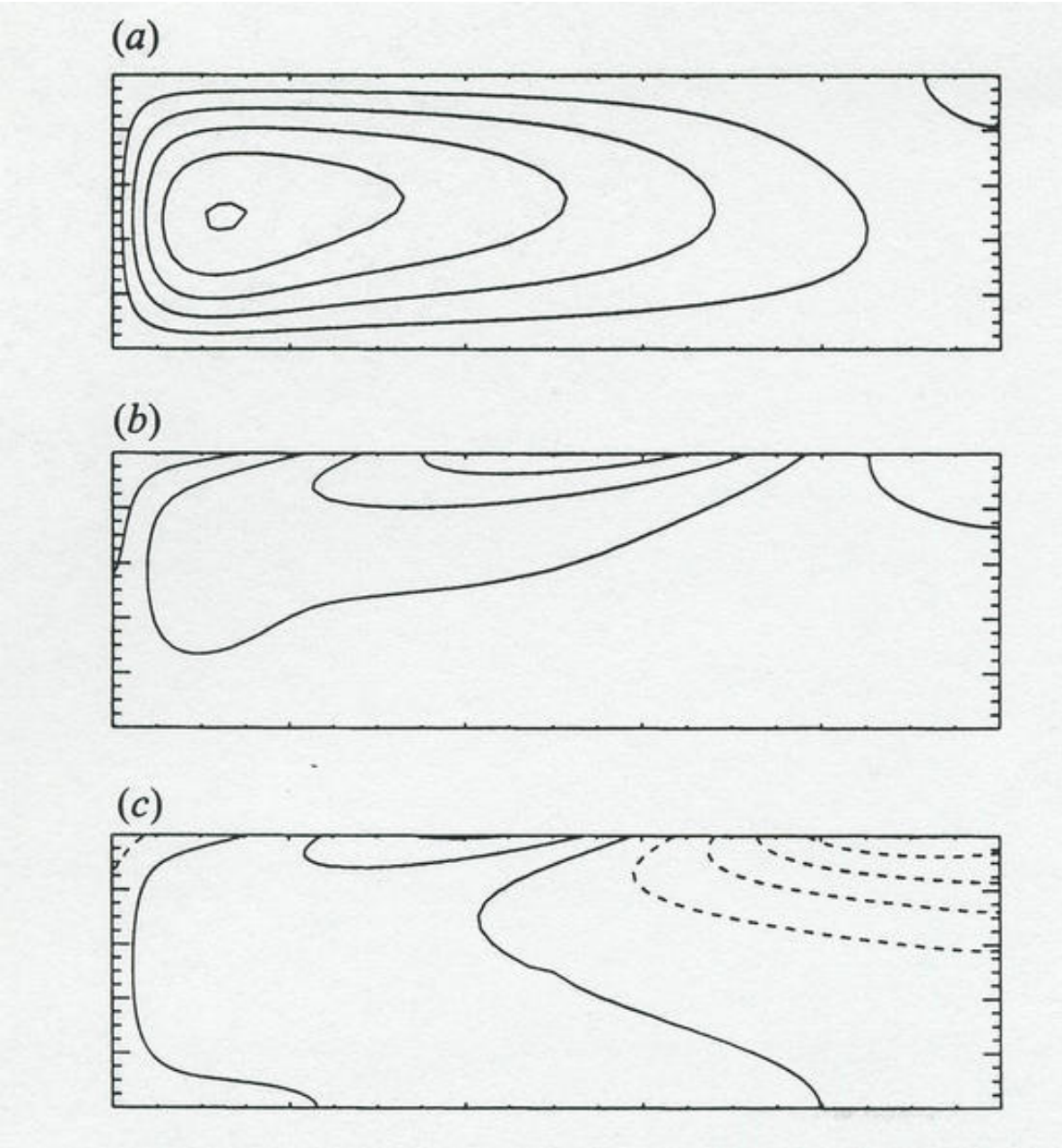

Figure 25: Pole-to-pole steady state of a 2D fluid model at the Hopf bifurcation point: (a) stream-function, (b) T, and (c) S (Dijkstra and Molemaker, 1997).

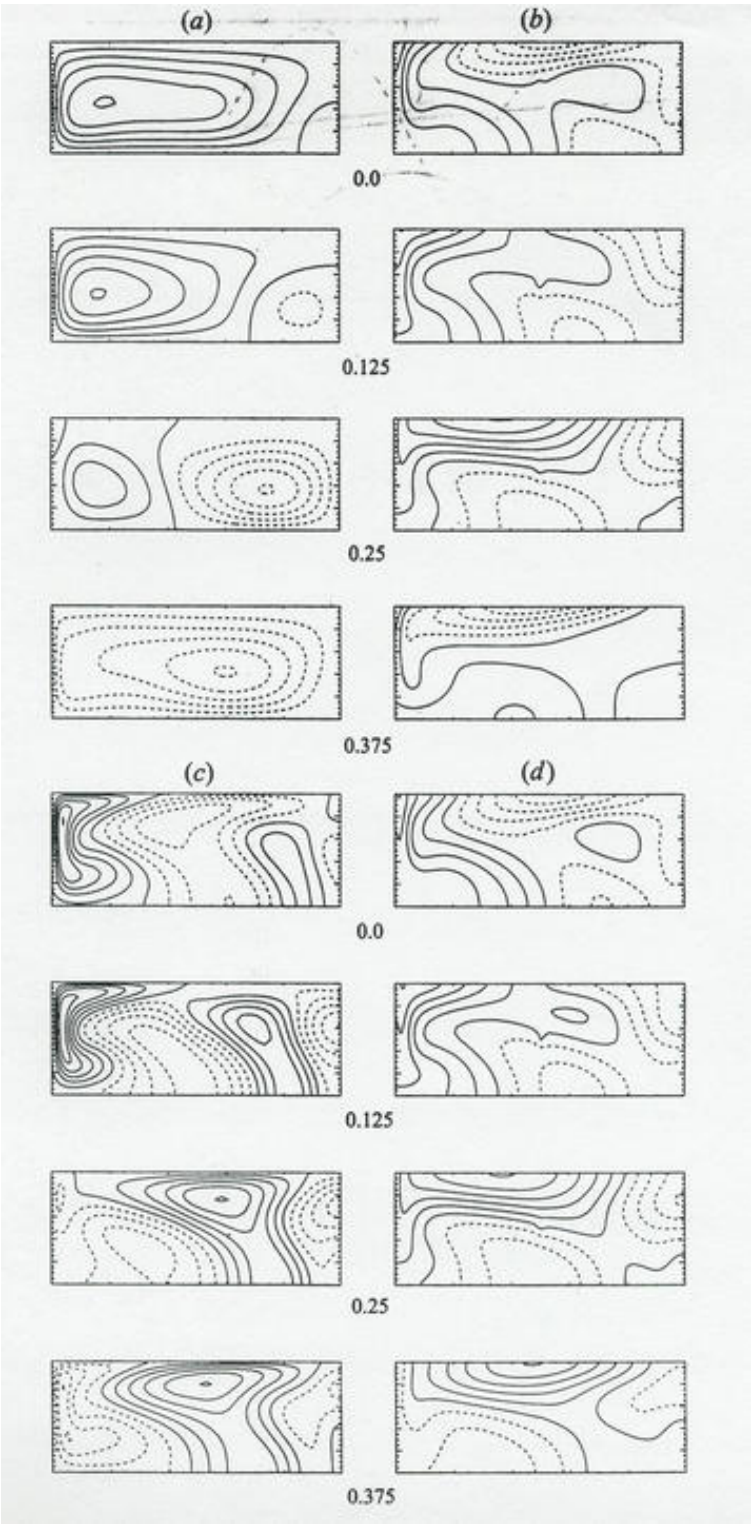

Figure 26: Periodically forced oscillation about the pole-to-pole steady state shown in Fig. 25 for a 2D fluid model: (a) streamfunction, (b) ρ, (c) T, (d) S shown at four different times $\omega t/2\pi$ during the periodic oscillation (Dijkstra and Molemaker, 1997).

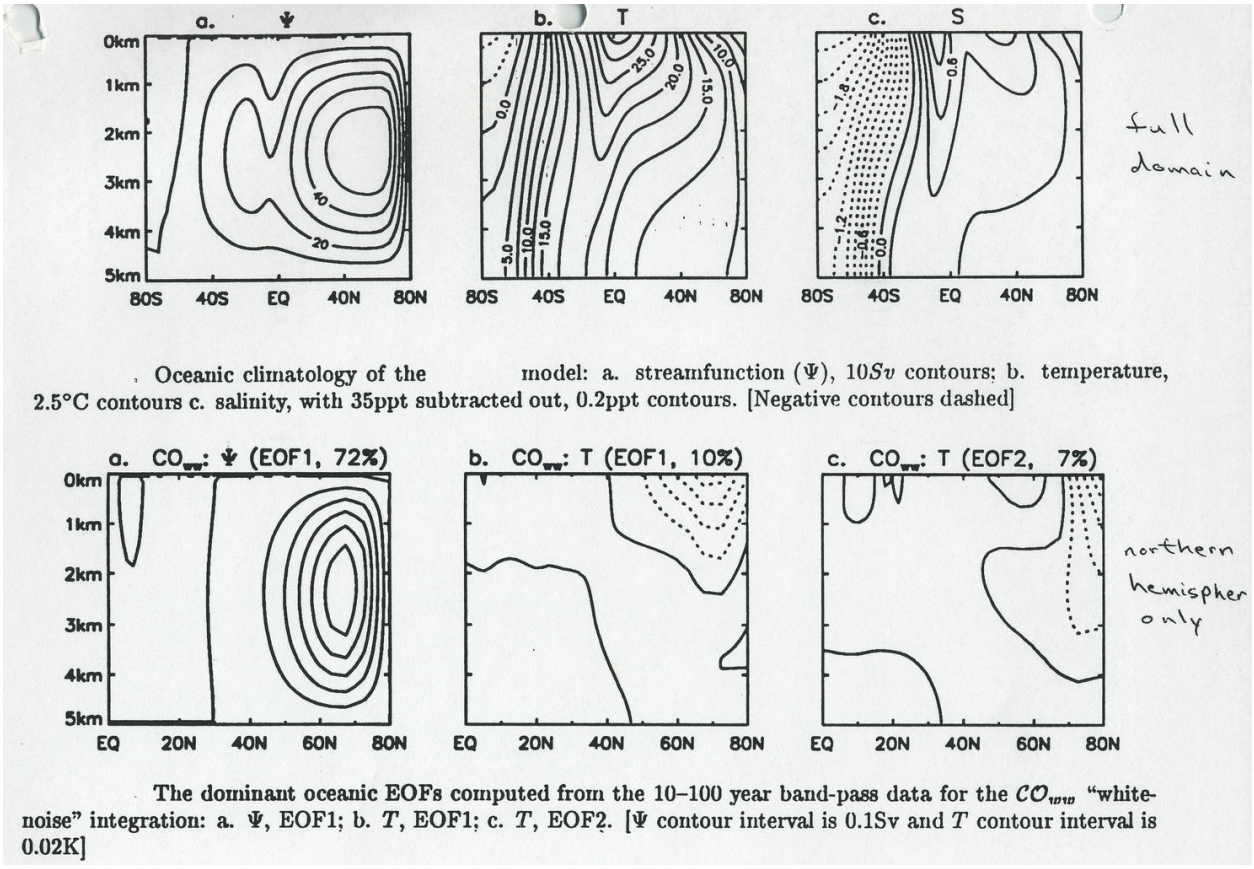

Figure 27: Time-mean and dominant EOF for the variability in a 2D fluid model with stochastic transient forcing (Saravanan and McWilliams, 1997).

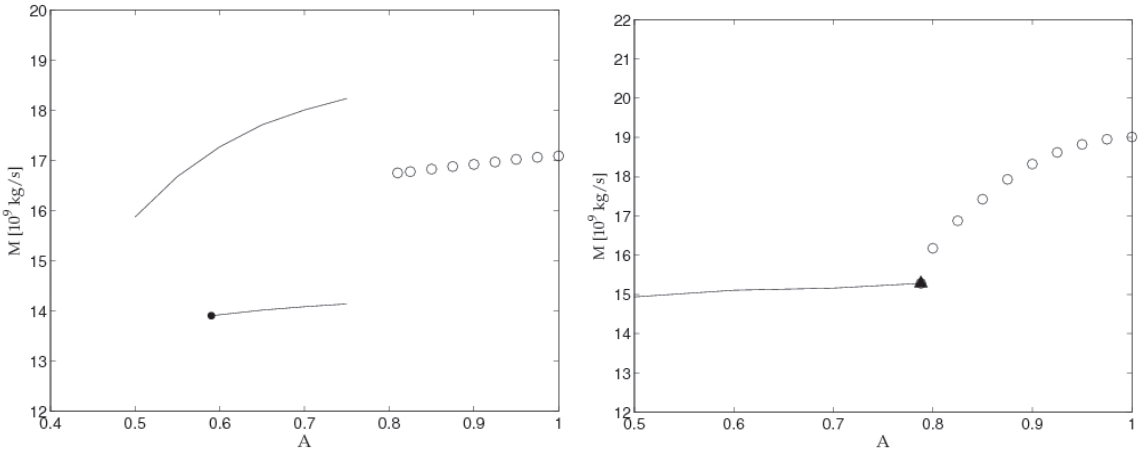

Figure 28: Bifurcation diagrams for steady solutions (solid lines) and decadal limit cycles (open circles) with (left) mixed surface boundary conditions and (right) flux boundary conditions. The black lines are incompletely delineated here, except at the point of the black circle where this solution branch terminates. The abscissa is proportional to the combined Rayleigh number Ra for heat and freshwater forcing, and the ordinate is the mass transport amplitude of the MOC (Molemaker and McWilliams, 2006).

References

Arzel, O., T. Huck, and A. Colin de Verdiere: 2006, Identifying two types of interdecadal variabilty of the thermohaline circulation. *J. Phys. Ocean.*, **36**, 1703–1718.

Bryan, F.: 1986, High-latitude salinity effects and interhemispheric thermohaline circulations. *Nature*, **323**, 301–304.

Colin de Verdiere, A.: 1976, On the interaction of wind and buoyancy driven gyres. *J. Mar. Res.*, **47**, 595–633.

Dijkstra, H. and M. Molemaker: 1997, Symmetry breaking and overtuning oscillations in thermohaline-driven flows. *J. Fluid Mech.*, **331**, 169–198.

Gent, P. and J. McWilliams: 1990, Isopycnal mixing in ocean circulation models. *J. Phys. Ocean.*, **20**, 150–155.

Gordon, A.: 1975, General ocean circulation. *Numerical Models of Ocean Circulation*, R. Reid, ed., Nat. Acad. Sci. Press, 39–53.

Kawasi, M.: 1987, Establishment of deep ocean circulation driven by deep-water production. *J. Phys. Ocean.*, **17**, 2294–2317.

Large, G., W. Danabasoglu, S. Doney, and J. McWilliams: 1997, Sensitivity to surface forcing and boundary layer mixing in a global ocean model: Annual-mean climatology. *J. Phys. Ocean.*, **27**, 2418–2447.

Lavender, K., R. Davis, and W. Owens: 2002, Observations of open-ocean deep convection in the Labrador Sea from subsurface floats. *J. Phys. Ocean.*, **32**, 511–526.

Ledwell, J., A. Watson, and C. Law: 1993, Evidence for slow mixing across the pycnocline from an open-ocean tracer-release experiment. *Nature*, **364**, 701–703.

Molemaker, M. and J. McWilliams: 2006, Decadal thermohaline oscillations. *Geophys. Astro. Fluid Dyn.*, submitted.

Munk, W.: 1966, Abyssal recipes. *Deep Sea Res.*, **13**, 707–730.

Munk, W. and C. Wunsch: 1998, Abyssal recipes II: energetics of tidal and wind mixing. *Deep Sea Res.*, **45**, 1977–2010.

Niiler, P.: 1992, The ocean circulation. *Climate System Modeling*, K. Trenberth, ed., Cambridge University Press, 117–148.

Östlund, H. and C. Rooth: 1990, North Atlantic tritium and radiocarbon transients. *J. Geophys. Res.*, **95**, 20147–20166.

Pedlosky, J.: 1987, Thermocline theories. *General Circulation of the Ocean*, H. Abarbanel and W. Young, eds., Springer-Verlag, 55–101.

— 1996, *Ocean Circulation Theory*. Springer-Verlag, 453 pp.

Price, J., M. O'Neil Baringer, R. Lueck, G. Johnson, I. Ambar, G. Parrilla, A. Cantos, M. Kennelly, and T. Sanford: 1993, Mediterranean outflow mixing and dynamics. *Science*, **259**, 1277–1282.

Samelson, R. and G. Vallis: 1997, Large-scale circulation with small diapycnal diffusion: The two-thermocline limit. *J. Mar. Res.*, **55**, 223–275.

Saravanan, R., G. Danabasoglu, S. Doney, and J. McWilliams: 2000, Decadal variability and predictability in the midlatitude ocean-atmosphere system. *J. Clim.*, **13**, 1073–1097.

Saravanan, R. and J. McWilliams: 1997, Stochasticity and spatial resonance in interdecadal climate fluctuations. *J. Clim.*, **10**, 2299–2320.

Smethie, W. and R. Fine: 2001, Rates of North Atlantic Deep Water formation calculated from chlorofluorcarbon inventories. *Deep Sea Res.*, **48**, 189–216.

Stommel, H.: 1961, Thermohaline convection with two stable regimes of flow. *Tellus*, **2**, 244–268.

Stommel, H. and A. Arons: 1960, On the abyssal circulation of the world ocean. I. Stationary planetary flow patterns on a sphere & II. An idealized model of the circulation pattern and amplitude in ocean basins. *Deep Sea Res.*, **6**, 140–154 & 202–206.

Thual, O. and J. McWilliams: 1992, The catastrophe structure of thermohaline convection in a two-dimensional fluid model and a comparison with low-order box models. *Geophys. Astro. Fluid Dyn.*, **64**, 67–95.

Veronis, G.: 1981, Dynamics of the large-scale ocean circulation. *Evolution of Physical Oceanography*, B. Warren, ed., MIT Press, 140–183.

Weaver, A., J. Marotzke, P. Cummings, and E. Sarachik: 1993, Stability and variability of the thermohaline circulation. *J. Phys. Ocean.*, **23**, 197–231.

Webb, D. and N. Suginohara: 2001, Vertical mixing in the ocean. *Nature*, **409**, 37.

Welander, P.: 1986, Thermohaline effects in the ocean circulation and related simple models. *Large-Scale Transport Processes*, J. Willebrand and D. Anderson, eds., Reidel Press, 163–200.